A&A 666, A143 (2022)
https://doi.org/10.1051/0004-6361/202243773
© D. Kossakowski et al. 2022

Astronomy & Astrophysics

The CARMENES search for exoplanets around M dwarfs

Stable radial-velocity variations at the rotation period of AD Leonis: A test case study of current limitations to treating stellar activity★

D. Kossakowski[1], M. Kürster[1], Th Henning[1], T. Trifonov[1,2], J. A. Caballero[3], M. Lafarga[4,5,6], F. F Bauer[7], S. Stock[8], J. Kemmer[8], S. V. Jeffers[9], P. J. Amado[7], M. Pérez-Torres[7], V. J. S. Béjar[10,11], M. Cortés-Contreras[3], I. Ribas[5,6], A. Reiners[12], A. Quirrenbach[8], J. Aceituno[7], D. Baroch[5,6], C. Cifuentes[3], S. Dreizler[12], A. Hatzes[13], A. Kaminski[8], D. Montes[14], J. C. Morales[5,6], A. Pavlov[1], L. Peña[7], V. Perdelwitz[15,16], S. Reffert[8], D. Revilla[7], C. Rodríguez López[7], A. Rosich[5,6], S. Sadegi[8,1], J. Sanz-Forcada[3], P. Schöfer[7,12], A. Schweitzer[16], and M. Zechmeister[12]

[1] Max-Planck-Institut für Astronomie, Königstuhl 17, 69117 Heidelberg, Germany
e-mail: diana.kossakowski@gmail.com
[2] Department of Astronomy, Sofia University "St Kliment Ohridski", 5 James Bourchier Blvd, 1164 Sofia, Bulgaria
[3] Centro de Astrobiología (CSIC-INTA), ESAC, Camino bajo del castillo s/n, 28692 Villanueva de la Cañada, Madrid, Spain
[4] Department of Physics, University of Warwick, Gibbet Hill Road, Coventry CV4 7AL, UK
[5] Institut de Ciències de l'Espai (ICE, CSIC), Campus UAB, C/ de Can Magrans s/n, 08193 Cerdanyola del Vallès, Spain
[6] Institut d'Estudis Espacials de Catalunya (IEEC), C/ Gran Capità 2–4, 08034 Barcelona, Spain
[7] Instituto de Astrofísica de Andalucía (CSIC), Glorieta de la Astronomía s/n, 18008 Granada, Spain
[8] Landessternwarte, Zentrum für Astronomie der Universität Heidelberg, Königstuhl 12, 69117 Heidelberg, Germany
[9] Max-Planck-Institut für Sonnensystemforschung, Justus-von-Liebig Weg 3, 37077 Göttingen, Germany
[10] Instituto de Astrofísica de Canarias (IAC), 38205 La Laguna, Tenerife, Spain
[11] Departamento de Astrofísica, Universidad de La Laguna, 38206 La Laguna, Tenerife, Spain
[12] Institut für Astrophysik, Georg-August-Universität, Friedrich-Hund-Platz 1, 37077 Göttingen, Germany
[13] Thüringer Landessternwarte Tautenburg, Sternwarte 5, 07778 Tautenburg, Germany
[14] Departamento de Física de la Tierra y Astrofísica & IPARCOS-UCM (Instituto de Física de Partículas y del Cosmos de la UCM), Facultad de Ciencias Físicas, Universidad Complutense de Madrid, 28040 Madrid, Spain
[15] Department of Physics, Ariel University, Ariel 40700, Israel
[16] Hamburger Sternwarte, Gojenbergsweg 112, 21029 Hamburg, Germany

Received 13 April 2022 / Accepted 31 August 2022

ABSTRACT

Context. A challenge with radial-velocity (RV) data is disentangling the origin of signals either due to a planetary companion or to stellar activity. In fact, the existence of a planetary companion has been proposed, as well as contested, around the relatively bright, nearby M3.0 V star AD Leo at the same period as the stellar rotation of 2.23 days.

Aims. We further investigate the nature of this signal. We introduce new CARMENES optical and near-IR RV data and an analysis in combination with archival data taken by HIRES and HARPS, along with more recent data from HARPS-N, GIANO-B, and HPF. Additionally, we address the confusion concerning the binarity of AD Leo.

Methods. We consider possible correlations between the RVs and various stellar activity indicators accessible with CARMENES. We additionally applied models within a Bayesian framework to determine whether a Keplerian model, a red-noise quasi-periodic model using a Gaussian process, or a mixed model would explain the observed data best. We also exclusively focus on spectral lines potentially associated with stellar activity.

Results. The CARMENES RV data agree with the previously reported periodicity of 2.23 days, correlate with some activity indicators, and exhibit chromaticity. However, when considering the entire RV data set, we find that a mixed model composed of a stable and a variable component performs best. Moreover, when recomputing the RVs using only spectral lines insensitive to activity, there appears to be some residual power at the period of interest. We therefore conclude that it is not possible to determinedly prove that there is no planet orbiting in synchronization with the stellar rotation given our data, current tools, machinery, and knowledge of how stellar activity affects RVs. We do rule out planets more massive than 27 $M_{\oplus}$ (=0.084 $M_{\rm Jup}$). Likewise, we exclude any binary companion around AD Leo with $M \sin i$ greater than 3–6 $M_{\rm Jup}$ on orbital periods <14 yr.

Key words. techniques: radial velocities – stars: late-type – stars: individual: AD Leonis – stars: activity

★ Tables A.2, A.3, A.4, A.5, and additional data (i.e., stellar activity indicators as shown in Figs. C.1, C.2, and C.3) are available at the CDS via anonymous ftp to cdsarc.u-strasbg.fr (130.79.128.5) or via http://cdsarc.u-strasbg.fr/viz-bin/cat/J/A+A/666/A143

1. Introduction

In the pursuit for Earth-like planets, modern spectrographs are pushing the limits by reaching m s^{-1} level precision or even tens

Open Access article, published by EDP Sciences, under the terms of the Creative Commons Attribution License (https://creativecommons.org/licenses/by/4.0), which permits unrestricted use, distribution, and reproduction in any medium, provided the original work is properly cited.
This article is published in open access under the Subscribe-to-Open model. Open access funding provided by Max Planck Society.

of cm s^{-1} (e.g., ESPRESSO; Pepe et al. 2021), which is needed. However, the measurements begin to succumb to unwanted signals for planet searches. Intrinsic stellar variability in the form of dark spots, bright plages, and flares can produce radial-velocity (RV) variations that can conceal true planetary signals, or even masquerade as a fake planet which then can be effectively modeled with a Keplerian orbit. To help mitigate these stellar-activity-induced RV signals, a number of procedures are commonly put in place, such as different modeling approaches, smart data collection strategies, and extraction of particular spectral lines.

Statistical techniques such as Gaussian process (GP) regression have been used by treating stellar activity behavior as a quasi-periodic signal (e.g., Haywood et al. 2014; Rajpaul et al. 2015; Jones et al. 2017). This approach may sometimes lead to better precision and accuracy of planetary parameters, especially those in the lower-mass regime (e.g., Stock et al. 2020; Amado et al. 2021). Likewise, these signals can be wavelength-dependent, usually with the amplitude decreasing in the redder regime of the spectrum, but still containing some residual effect depending on the star-spot configuration and temperature difference (Reiners et al. 2010, and references therein). For this reason, there is a push for higher-precision instruments covering the red and near-IR wavelength range such as CARMENES[1] (Quirrenbach et al. 2014, 2018), GIARPS[2] (Claudi et al. 2017), HPF[3] (Mahadevan et al. 2012, 2014), IRD[4] (Tamura et al. 2012; Kotani et al. 2014, 2018), MAROON-X[5] (Seifahrt et al. 2018, 2020), and SPIRou[6] (Donati et al. 2020).

Focusing on certain spectral lines as activity indicators sensitive to chromospheric (e.g., Hα, Ca II infrared triplet) or photospheric (e.g., TiO) effects on active M dwarfs can oftentimes be successful in determining the star's rotational period (see Fig. 11 in Schöfer et al. 2019). Even then, there is no universal approach because it is still not unique as to which activity indices do peak at the rotational period and under what conditions, as pointed out by Lafarga et al. (2021). Moreover, efforts for identifying which spectral lines, in general (i.e., not focusing on already-known specific lines), seem to be more activity-sensitive than others have been fruitful for a selection of G–K dwarfs (e.g., Wise et al. 2018; Dumusque 2018; Lisogorskyi et al. 2019; Ning et al. 2019; Cretignier et al. 2020; Thompson et al. 2020). Such an approach proves to be rather challenging for M dwarfs, where the spectra contain a forest of blended lines, making it almost impossible to find the continuum (Merrill et al. 1962; Boeshaar 1976; Kirkpatrick et al. 1991; Alonso-Floriano et al. 2015). This approach, however, seems to have been successful for stars that show a clear stellar activity impact on the RVs (e.g., EV Lac, Lafarga priv. comm.).

We turn our attention specifically to the active mid-type M dwarf AD Leo, a star whose stellar rotation period of 2.23 days presents itself both in photometry and RVs (Morin et al. 2008; Tuomi et al. 2018; Carleo et al. 2020; Robertson et al. 2020). Despite its strong flaring activity manifesting itself at many wavelengths (Buccino et al. 2007; Rauer et al. 2011; Tofflemire et al. 2012; Vidotto et al. 2013), AD Leo has been included in a number of studies addressing the existence of planets orbiting this star. Tuomi et al. (2018), referred to as T18 hereinafter, first suggested that a planet may be orbiting AD Leo in a 1:1 spin-orbit resonance since it proved to be difficult to simultaneously explain both the photometry and RV measurements using a variety of star-spot scenarios. Furthermore, they claimed that the RV measurements were time- and wavelength-independent, and the putative planet exhibited a semi-amplitude of ~19 m s^{-1}. Despite some evidence for solely stellar activity behavior, T18 concluded that AD Leo is an active M dwarf hosting a hot Jupiter ($\geq$0.2 $M_{\rm Jup}$) in a 1:1 spin-orbit resonance.

However, the existence of this hot Jupiter around AD Leo was challenged. Carleo et al. (2020, referred to as C20 hereinafter) investigated the 2.23 days signal and obtained observations with GIARPS at the 3.56 m Telescopio Nazionale *Galileo* (Claudi et al. 2017). Even though the 2.23 days signal was persistent, the amplitude heavily diminished as a function of wavelength and of time. Simultaneous photometric data from STELLA showed a shift of ~0.25 in phase (~0.6 days) in comparison to the HARPS-N RV curves. Therefore, C20 disputed the argument posed by T18, concluding that the RV modulation is not compatible with a planetary companion. Shortly after, the conclusions by Robertson et al. (2020), referred to as R20 hereinafter, were also in line with C20, as they likewise observed a decrease in amplitude between the two observing seasons using HPF spectroscopic data. At the time of submission, additional data from SPIRou and SOPHIE[7] also indicated no evidence for a corotating planet (Carmona et al., in prep.).

This concept of such a hot Jupiter around an M dwarf in a synchronized rotation is unique. Many studies addressing the correlation between the orbital period ($P_{\rm orb}$) and the stellar rotation period ($P_{\rm rot}$) have thus far been focused on more solar-like transiting host stars rather than M dwarfs, using *Kepler* data (Borucki et al. 2010). Findings from McQuillan et al. (2013) and Walkowicz & Basri (2013) suggest a clear absence of close-in planets ($P_{\rm orb} \lesssim$ 2–3 days) around rapidly rotating stars ($P_{\rm rot} \lesssim$ 5–10 days), where planets with shorter periods were nearly synchronous ($P_{\rm orb} \sim P_{\rm rot}$). Teitler & Königl (2014) proposed that the cause was orbital decay of close-in planets by their host stars. Besides, with regards to M dwarfs, Newton et al. (2016) showed that typical stellar rotation periods would often match the periods of planets in their habitable zone. Regardless, there is a dearth of close-in massive planets around M dwarfs where only a handful of such are known, such as NGST-1 b (Bayliss et al. 2018) or TOI-519 b ($M \lesssim 14\,M_{\rm Jup}$; Parviainen et al. 2021). This is not a result of observational bias as these types of planets would be simple to detect through transits and precise RVs. AD Leo was even used as a test case to check the effects of XUV irradiation on planet atmospheres (Chadney et al. 2016), considering that the ionsphere can play an influential role in regulating the stability of upper atmospheres on giant planets. Therefore, understanding the case of AD Leo could aid in finding the key methods for other potential planet detections that suffer from ambiguities due to 1:1 spin-orbit resonances.

[1] Calar Alto high-Resolution search for M dwarfs with Exo-earths with Near-infrared and optical Échelle Spectrographs, http://carmenes.caha.es

[2] GIAno & haRPS-n, https://www.tng.inaf.it/news/2017/04/04/giarps/

[3] The Habitable Zone Planet. Finder, https://hpf.psu.edu/

[4] InfraRed Doppler instrument.

[5] Red-optical, high-resolution spectrograph with focus on mid- to late-type M dwarfs, https://www.gemini.edu/instrumentation/maroon-x/

[6] A near-infrared spectropolarimeter/velocimeter, https://spirou.omp.eu/

[7] Optical échelle spectrograph, http://www.obs-hp.fr/guide/sophie/sophie-eng.shtml

In our focused study using optical and near-IR RV measurements, we claim that one cannot prove (or disprove) the suggested planetary signal in the AD Leo system, as the problem is completely degenerate and we are limited by our current state-of-the-art machinery and measurements. We organize the paper as follows. In Sect. 2, we first introduce the active M dwarf AD Leo and investigate its presumed binarity for the first time. All available RV data used for the analysis are presented in Sect. 3. We turn our focus on the chromaticity of the RV signal for the CARMENES data in Sect. 4. Still concentrating on the CARMENES data, in Sect. 5 we perform a spectral line analysis for the target. Then combining all available spectroscopic data for the first time, we explore various modeling techniques within the Bayesian framework in Sect. 6. Finally, in Sect. 7, we present a discussion on our results as well as suggestions to break the degeneracy of this situation. We summarize our conclusions in Sect. 8.

2. AD Leo

2.1. Stellar parameters

AD Leo (GJ 388), an M3.0 V star at a distance of slightly less than 5 pc and with $V \sim 9.5$ mag, is one of the closest and brightest M dwarfs. Already tabulated in the Bonner Sternverzeichnis by Argelander (1861), AD Leo has been the subject of numerous investigations in the last century (e.g., Abell 1959; Engelkemeir 1959; Lang et al. 1983; Saar & Linsky 1985; Hawley & Pettersen 1991; Hawley et al. 2003; Osten & Bastian 2008; Hunt-Walker et al. 2012).

In Table 1, we list the stellar properties of AD Leo. In particular, we tabulate equatorial coordinates, proper motions, and parallax from the *Gaia* Early Data Release 3 (EDR3; Gaia Collaboration 2021) and absolute RV from Lafarga et al. (2020, uncorrected of gravitational redshift for consistency with the previous literature), from which we recompute Galactocentric space velocities as in Cortés-Contreras (2016). The spectral type of Alonso-Floriano et al. (2015) superseded previous determinations (e.g., Johnson & Morgan 1953; Bidelman 1985; Stephenson 1986; Keenan & McNeil 1989), while the photosphere parameters of Passegger et al. (2019) match previous CARMENES publications and are similar, but not identical, to those of Rojas-Ayala et al. (2012), Lépine et al. (2013), Gaidos et al. (2014), or Mann et al. (2015). With the effective temperature of Passegger et al. (2019), the bolometric luminosity of Cifuentes et al. (2020), and the Stefan-Boltzmann law we derived the stellar radius and, with the radius-mass relation of Schweitzer et al. (2019), the stellar mass. For compiling the most precise parameters of the activity indicators, we used the `SVO Discovery Tool`[8]. The projected rotational velocity $v \sin i$ was computed by us exactly as in Reiners et al. (2018), but on the newest CARMENES template spectra (Sect. 3).

As first reported by Montes et al. (2001), the Galactocentric space velocity of AD Leo is consistent with it belonging to the Galactic young disk (Leggett 1992). Later, López-Santiago et al. (2010) and Klutsch et al. (2014) proposed AD Leo as a candidate member of the Castor moving group, in agreement with our latest kinematic data. The age of the Castor moving group, of about 300–500 Myr (Barrado y Navascués 1998; Mamajek et al. 2013), is consistent with age determinations for AD Leo by Shkolnik et al. (2009), Brandt et al. (2014), and Meshkat et al. (2017).

[8] http://sdc.cab.inta-csic.es/SVODiscoveryTool/

Table 1. Stellar parameters of AD Leo.

Parameter	Value	Reference
	Identifiers	
BD	+20 2465	Arg1861
Ci	18 1244	Por1915
GJ	388	Gli1957
Karmn	J10196+198	Cab2016
	Astrometry and kinematics	
α (epoch J2016.0)	10:19:35.7	*Gaia* EDR3
δ (epoch J2016.0)	19:52:11.3	*Gaia* EDR3
$\mu_\alpha \cos\delta$ (mas yr^{-1})	-498.62 ± 0.03	*Gaia* EDR3
μ_δ (mas yr^{-1})	-43.43 ± 0.03	*Gaia* EDR3
π (mas)	201.41 ± 0.03	*Gaia* EDR3
d (pc)	4.964 ± 0.001	*Gaia* EDR3
γ (km s^{-1})	12.286 ± 0.021	Laf2020
U (km s^{-1})	-14.929 ± 0.010	This work
V (km s^{-1})	-7.444 ± 0.007	This work
W (km s^{-1})	$+3.391 \pm 0.017$	This work
Galactic population	Young disk	Mon2001
Stellar kinematic group	Castor	LS2010
	Key photometry	
G (mag)	8.2041 ± 0.0015	*Gaia* EDR3
J (mag)	5.449 ± 0.027	2MASS
	Photospheric parameters	
Spectral type	M3.0 V	AF2015
$T_{\rm eff}$ (K)	3477 ± 23	Mar2021
$\log g$ (cgs)	5.12 ± 0.12	Mar2021
[Fe/H] (dex)	-0.19 ± 0.12	Mar2021
<Bf> (G)	3357 ± 172	Rein2022
	Activity	
$v \sin i$ (km s^{-1})	2.4 ± 1.5	This work$^{(a)}$
$P_{\rm rot}$ (d)	$2.2270^{+0.0010}_{-0.0011}$	This work$^{(b)}$
pEW(Hα) (Å)	-3.73 ± 0.41	Fuhr2022
$\log {\rm H}\alpha/L_{\rm bol}$	-3.614 ± 0.003	Sch2019
$\log R'_{\rm HK}$	-3.97 ± 0.05	This work
$\log L_{\rm X}/L_{\rm bol}$	-3.3	Fav2000
	Physical parameters	
$L_\star$ ($10^{-5}\,L_\odot$)	2359 ± 11	This work
$R_\star$ ($R_\odot$)	0.4233 ± 0.0057	This work
$M_\star$ ($M_\odot$)	0.423 ± 0.012	This work
i (deg)	$12.9^{+8.4}_{-8.1}$	This work

Notes. $^{(a)}$This value was individually produced for AD Leo using a chosen order selection and is consistent, but supersedes previous measurement (e.g., Marfil et al. 2021). $^{(b)}$See Sect. 6.3 for the $P_{\rm rot}$ determination and Table A.1 for other rotational periods found in the literature.

References. 2MASS: Skrutskie et al. (2006); AF2015: Alonso-Floriano et al. (2015); Arg1861: Argelander (1861); Cab2016: Caballero et al. (2016); Fav2000: Favata et al. (2000); Fuhr2022: Fuhrmeister et al. (2022); *Gaia* EDR3: Gaia Collaboration (2021); Gli1957: Gliese (1957); Hoj2019: Hojjatpanah et al. (2019); Laf2020: Lafarga et al. (2020); LS2010: López-Santiago et al. (2010); Mar2021: Marfil et al. (2021); Mon2001: Montes et al. (2001); Rein2022: Reiners et al. (2022); Pass2019: Passegger et al. (2019); Por1915: Porter et al. (1915); Sch2019: Schöfer et al. (2019).

Such a young age partly explains the flares frequently observed in AD Leo. The star has been known to exhibit activity ever since the first observed optical flare event in 1949

(Gordon & Kron 1949), followed by many others (e.g., Liller 1952; MacConnell 1968; Pettersen et al. 1984; Crespo-Chacón et al. 2006)[9]. Frequent flaring activity was further observed during an extreme ultraviolet (EUV) 1-month monitoring of AD Leo (Sanz-Forcada & Micela 2002). Later on, emission in the X-ray and radio regimes has also been observed (Gurzadyan 1971; Robinson et al. 1976), and which has shown bursting radio emission at GHz frequencies and below (Osten & Bastian 2008; Villadsen & Hallinan 2019). Muheki et al. (2020) and Namekata et al. (2020) have presented the most recent analyses on high-resolution optical spectroscopy and X-ray observations of flares on AD Leo.

The young age of AD Leo also explains the moderately large rotational velocity and short rotational period, of 2.23 days, as well as X-ray, Ca II H&K, and Hα emission (see references in Table 1). In addition, this star presents large RV variations: it shows a standard deviation larger than 20 m s^{-1}, (~1.5× median absolute deviation RV as in Tal-Or et al. 2019 and Grandjean et al. 2020), which can be connected to stellar activity, the presence of a planetary companion, or both. For the derivation of $\log R'_{\rm HK}$, we used the method described by Perdelwitz et al. (2021), albeit with a slight modification of the $k1$ passband used for normalization. A total of 316 archival spectra from ESPaDOnS (232 spectra), HARPS (58 spectra), HIRES (24 spectra) and NARVAL (2 spectra) were analyzed, yielding a mean value of $\log R'_{\rm HK} = -3.97 \pm 0.05$, which is in agreement with the result published by Astudillo-Defru et al. (2017) based on the HARPS spectra alone. We compute the stellar inclination, i, to be ~13° from 10^6 MCMC realizations using $v \sin i$, R, and $P_{\rm rot}$ as provided in the stellar parameters table. Previous papers quoted values of ~20° (Morin et al. 2008) and ~15° (Tuomi et al. 2018).

2.2. Photometric rotational period

T18 took a closer look at the available photometry from ASAS-North and ASAS-South, as well as from short-cadence *MOST* observations (see T18 for photometry references). To summarize, the ASAS photometry shows a long-term periodicity of around 4070 days, most likely due to a stellar activity cycle. During the brightness minimum of this cycle, the signal at the rotation period of 2.23 days seems to disappear turning up only during the brightness maximum, in which the *MOST* observations were taken. These short-cadence *MOST* data, taken over the course of 9 days (Hunt-Walker et al. 2012), showed fluctuations with periodicity 2.23 days, but also demonstrated behavior of slight phase shifts and amplitude and period variations, indicating that the stellar surface should be experiencing rapid evolution. Other observations taken with different instruments are in agreement with the 2.23 days period (see Table A.1).

AD Leo was additionally observed in three of the TESS sectors[10], particularly in sector 45 (camera #3 CCD #4; 6 November 2021 to 02 December 2021), sector 46 (camera #2 CCD #2; 02 December 2021 to 30 December 2021), and in sector 48 (camera #1 CCD #4; 28 January 2022 to 26 February 2022). All sectors constitute short cadence 20-second and 2-minute integrations. Unfortunately, the pixel column was saturated for sectors 45 and 46 leading to unusable data. The sector 48 data were still valuable for determining a periodic variation. In doing so, we removed strong flare events (up to 275 ppt) and any outliers on the 20-second integration data which were binned every 10 points for computational reasons. After applying a sinusoid model, the resulting amplitude and $P_{\rm rot}$ are ~800 ppm and $P_{\rm rot}$ of 2.2304 ± 0.0014 days, respectively.

2.3. Hypothetical binary

There is some confusion in the literature regarding the hypothetical multiplicity of AD Leo. First of all, in spite of being listed as "γ Leo C" in some astronomical databases (e.g., SIMBAD), AD Leo is not a wide ($\rho \sim 5.7$ arcmin) physical companion to Algieba, which is a binary system of two G- and K-type giant stars visible to the naked-eye located eight times further (γ^{01}Leo+γ^{02} Leo; van Leeuwen 2007; Gaia Collaboration 2021).

Next, the Washington Double Star (WDS; Mason et al. 2001) catalog tabulates AD Leo as a close binary candidate. The presence of a hypothetical companion around AD Leo was first inferred by Reuyl (1943) from measurements of photographic plate images. He suggested an eccentric (e = 0.6) and close-in (a ~ 0.54 au, projected angular separation of ρ ~ 0.11 arcsec) orbit with an orbital period of 26.5 yr, making the companion a brown dwarf ($M \approx 0.032\,M_\odot$). Later, van de Kamp & Lippincott (1949) found indications of an astrometric trend from photographic plates that did not fit those orbital elements. Following up two decades later, Lippincott (1969) found an ambiguous deviation from linear proper motion, thus deciding that it was inconclusive to determine whether there could be a variable proper motion due to a companion.

With speckle imaging at 7800 Å at the 3.6 m Canada–France–Hawai'i Telescope, Balega et al. (1984) resolved a companion candidate to AD Leo at $\rho = 0.078 \pm 0.010$ arcsec ($r \approx$ 0.39 au) and position angle of $\theta = 39 \pm 4$ deg in 1981, which received the WDS name 10200+1950 and discoverer code BAG 32. Two additional measurements in 1983 were provided by Balega & Balega (1985) at ρ ~ 0.11 arcsec, but with θ ~ 330 deg. Afterwards, with lucky imaging in the I band at the 1.5 m Telescopio *Carlos Sánchez*, Cortés-Contreras et al. (2017) resolved a candidate source, about 2.0 mag fainter than AD Leo, at $\rho = 0.195 \pm 0.061$ arcsec ($r \approx$ 0.97 au) and $\theta = 23.8 \pm 3.7$ deg in 2012. However, it fell on the first Airy disk, and they were not able to detect it again in observations in 2015 with the same instrument setup. From $\Delta I \approx 2.0$ mag and the projected physical separation of about 0.97 au, Cortés-Contreras et al. (2017) estimated an M5 V spectral type for the companion candidate and an orbital period of P ~ 1.5 yr, which might be the source discovered by Balega et al. (1984). Because of this hypothetical companion, AD Leo was initially discarded from the CARMENES guaranteed time observation target list (Caballero et al. 2016; Reiners et al. 2018).

Further attempts at resolving the companion proved to be unsuccessful, such as additional speckle imaging by Docobo et al. (2006). With adaptive optics at 8 m-class telescopes, Daemgen et al. (2007) and Brandt et al. (2014) imposed very strict upper limits to the presence of companions, of $\Delta K_{\rm s}$ ~ 7.8 mag at $\rho \geq 0.5$ arcsec and ΔH ~ 10.9 mag at $\rho \geq 1.5$ arcsec, respectively. From Fig. 7 in Daemgen et al. (2007), their Altair/Gemini North observations discarded any companion of $\Delta K_{\rm s}$ ~ 2.0 mag at $\rho \geq 0.1$ arcsec. No trace of companions is seen either in archival images obtained in 2005 with the *Hubble* Space Telescope (ACS/HRC in F330W) and in 2018 with the Very Large Telescope (SPHERE in H)[11]. Therefore, the findings of Balega et al. (1984), Balega & Balega (1985), and

[9] Of the 70 reports of the IAU Information Bulletin on Variable Stars citing AD Leo, only 18 did not have the star name in the title.

[10] TESS Web Viewing Tool: https://heasarc.gsfc.nasa.gov/cgi-bin/tess/webtess/wtv.py, accessed 6 April 2022.

[11] Near-infrared archival images obtained in 1999 with *Hubble* NICMOS/NIC2 and in 2009 with VLT NAOS+CONICA saturate and are not useful at very close separations.

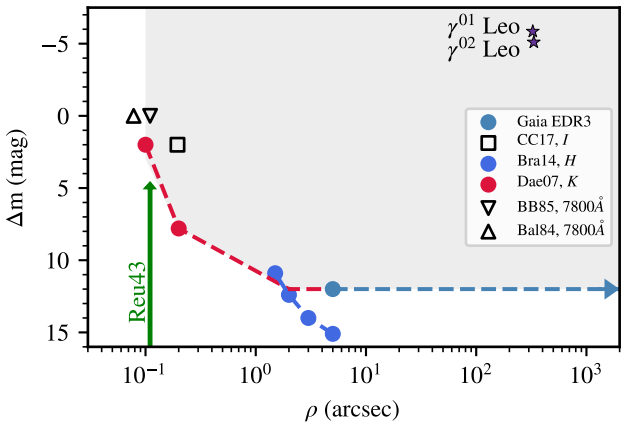

Fig. 1. Magnitude difference versus projected angular separation diagram for observations of potential companions around AD Leo. Detections should be above and to the right of the lines (gray shaded region). Inaccurate detection claims are indicated with open symbols. Measurements from *Gaia* EDR3 are indicated with an extended arrow to the right to demonstrate it continues for many more arcseconds. The upwards green arrow represents a rough difference in magnitude interval from the astrometric masses indicated by Reuyl (1943), which are difficult to pinpoint as they are subject to huge uncertainties. The bright binary γ Leo in the background of AD Leo is discussed in Sect. 2.3. References: CC17: Cortés-Contreras et al. (2017); Bra14: Brandt et al. (2014); Dae07: Daemgen et al. (2007); BB85: Balega & Balega (1985); Bal84: Balega et al. (1984); Reu43: Reuyl (1943), astrometry; *Gaia* EDR3: Gaia Collaboration (2021), astrometry.

Cortés-Contreras et al. (2017) are most probably not related to a real physical companion, unless the orbital motion can explain the later nondetections. Furthermore, the *Gaia* EDR3 renomalized unit weight error (`RUWE`) for AD Leo is 1.15, below the critical threshold of 1.40, the along-scan observations (`astrometric_gof_al`) is 3.22, and the excess noise of the source (`astrometric_excess_noise`) is 0.16, all of which indicate that it is most likely a single source (Lindegren et al. 2018). To rule out any wide companions, we searched for objects with common parallax and proper motions up to a projected physical separation of 100 000 au, as in Caballero et al. (2022), and found no hints of any wide potential companion. Figure 1 illustrates all the mentioned findings from the literature. The binary issue was not addressed by T18, C20, or R20. The absence of any close companion to AD Leo is further investigated with our spectroscopic data in Sect. 2.4.

2.4. Evidence for single star in spectroscopic data

As a first approach to search to address the potential stellar binarity and look for traces of it, we combined all the RV data (presented in Sect. 3) to look for long-term trends. However, this method presents its challenges as there is no temporal overlap between the older and newer data sets and each instrument has its own, unknown zero-point offset. We nonetheless attempted a grid search for a Keplerian signal for which we stepped through the period, amplitude, eccentricity and argument of periastron parameter space, where each instrument also had its own offset and jitter term[12] (e.g., Baluev 2009). One then adapts the values with the best log likelihood. Unfortunately, the lack of temporal overlap led to strong ambiguities and degeneracies. We therefore did not find any conclusive periodicity or indicative linear trend in this RV analysis.

We continued to investigate whether there is evidence for the presence of a companion within our CARMENES spectra that could affect the analysis presented later in this work. We computed a 1D cross-correlation function (CCF) with a binary mask over a large RV range and did not find any hint of a clear secondary peak, neither in the VIS nor the NIR data. To be certain, we also ran `todcor` (Zucker & Mazeh 1994), which computes a 2D CCF to get the RVs of the two components simultaneously, and the results showed no evidence for a companion as well. The 2D CCF method with `todcor` is well suited in the case of double-lined binaries, but since the secondary signal seems to be either too weak if expected to be $\sim$10 km s^{-1} away from the primary, or too hidden if expected to be very close to the primary, we concluded that no secondary heavily distorts the CCF profile and, therefore, would not cause any noticeable effects on the CCF parameter values. Therefore, we first discard the presence of a nearly equal brightness double-lined spectroscopic binary from the `todcor` analysis. Secondly, based on our RV time series analysis, we rule out companions with minimum masses greater than 3–6 $M_{\rm Jup}$ using orbital periods of less than $\sim$2–14 yr and amplitudes 3–5 greater than the rms of the earlier data set instruments (i.e., HARPS, HIRES), while assuming $\sin i \neq 0$. We therefore conclude that there is no evidence for a stellar binary or brown dwarf companion of AD Leo within this parameter regime.

2.5. Bursting radio emission from the AD Leo system

Radio bursts from AD Leo have been known for quite a long time, and have been ascribed to (coherent) plasma emission (Stepanov et al. 2001; Osten & Bastian 2008). More recently, Villadsen & Hallinan (2019) detected both short-duration (seconds to minutes) and long-duration (30 min or more) bursts of AD Leo, using ultrawide-band VLA observations (in the ranges 0.2–0.5 GHz and continuous frequency coverage between 1 and 6 GHz) in several epochs between 2013 and 2015. The timescale of the short-duration events was consistent with the duration of "space-weather" events, such as the impulsive phase of a flare or a coronal mass ejection (CME) crossing the corona. The long-duration bursts, which lasted hours, and possibly extended for up to days or even longer times, between observing epochs (similarly to the case of Proxima Centauri; see, e.g., Pérez-Torres et al. 2021 and references therein) require an ongoing electron acceleration mechanism during the burst. Candidate acceleration processes are found within the paradigms of solar radio bursts and periodic radio aurorae produced by ultracool dwarfs and planets.

The emission mechanism responsible for the aurorae from stars and planets alike is the electron cyclotron maser (ECM) instability (Melrose & Dulk 1982), whereby plasma processes within the star (or planet) magnetosphere generate a population of unstable electrons that amplifies the emission. The characteristic frequency of the ECM emission is given by the electron gyrofrequency, $\nu_{\rm G} = 2.8\,B$ MHz, where B is the local magnetic field in the source region, in Gauss. ECM emission is a coherent mechanism that yields broadband ($\Delta\nu \sim \nu_{\rm G}/2$), highly polarized (sometimes reaching 100%), amplified nonthermal radiation. The long-duration bursts seen for AD Leo by (Villadsen & Hallinan 2019) between 1 and 6 GHz are characteristic of ECM emission, implying electron densities $\lesssim 10^9$ cm^{-3}, and originate in regions with field strengths of 0.36–2.1 kG (in fundamental emission) or 0.18–1.1 kG (if second harmonic). Since the surface

[12] Jitter terms are added in quadrature to the given error bars for each respective instrument.

Table 2. Summary of the extensive spectroscopic data set for AD Leo.

Instrument	CARMENES VIS		CARMENES NIR		HIRES	HARPS	HARPS-N		GIANO-B		HPF	
$\Delta\lambda$ (nm)	520–960		960–1710		500–620	380–690	390–680		970–2450		810–1280	
R	94 600		80 400		60 000	115 000	115 000		50 000		55 000	
Subset [(a)]	VIS1	VIS2	NIR1	NIR2			HT1	HT2	G1	G2	HPF1	HPF2
# of spectra	26	20	26	20	43	47	42	21	12	13	5	30
rms (m s^{-1})	18.54	15.63	16.44	13.61	20.74	24.23	21.97	10.51	17.92	18.41	19.01	6.68
Start date	Mar. 2018	Feb. 2020	Mar. 2018	Feb. 2020	Jun. 2001	Dec. 2003	Apr. 2018	Nov. 2018	Apr. 2018	May. 2008	Apr. 2018	Dec. 2018
End date	Apr. 2018	Feb. 2020	Apr. 2018	Feb. 2020	Dec. 2013	May. 2014	Jun. 2018	Jan. 2019	May. 2018	Jun. 2018	Apr. 2018	Feb. 2020

Notes. All instruments used for the analysis along with their wavelength range, spectral resolution, and number of spectra are listed. [(a)]A subset is treated effectively as an independent data set.

magnetic field of AD Leo is estimated to be of ≃3.36 kG (Reiners et al. 2022), the above field strengths are likely to occur relatively close to the star, at a height less than about one stellar radius.

Auroral cyclotron maser emission is powered by the acceleration of confined electrons with energies between ∼10 keV and up to 1 MeV energies. For substellar objects, the currents could be driven by the breakdown of rigid corotation of magnetospheric plasma with the object's magnetic field, for example, due to the interaction between a rotating magnetosphere and the interstellar medium. Corotation breakdown observed in a number of ultracool (UCD) dwarfs with periods less than about 3 h seem to be rotation powered, with radio powers of up to a few times 10^{13} erg s^{-1} Hz^{-1} (e.g., Turnpenney et al. 2017). AD Leo has a rotation period of ∼54 h. Assuming coronal parameters similar to radio-loud UCDs, any corotation breakdown in AD Leo will generate a radio power that is $\sim 6 \times 10^{11}$ erg s^{-1} Hz^{-1}, or less than about 100 μJy. Therefore, corotation breakdown, while is likely to contribute to the overall radio power observed from AD Leo, cannot account for the observed radio bursts, which reach peaks of tens of mJy at GHz frequencies (Villadsen & Hallinan 2019). A discussion of further potential mechanisms, such as star-planet interaction, to explain the measurements is continued in Sect. 7.2.3.

3. Spectroscopic data

The Doppler data that are used in our analysis are described below. All data and spectrograph descriptions are summarized in Table 2. Data used for the analysis are displayed in Fig. 2, along with the generalized Lomb-Scargle (GLS) periodograms (Zechmeister & Kürster 2009) of the data in Fig. 3.

3.1. CARMENES

The CARMENES instrument is located at the 3.5 m telescope at the Calar Alto Observatory in Spain. It is a dual arm instrument to produce RV measurements at optical (VIS) and near-infrared (NIR) wavelengths (Quirrenbach et al. 2014, 2018, see Table 2 for the instrument specifications). We obtained 26 spectra for AD Leo (Karmn J10196+198) over the time span of 25 days in 2018, notably 12 yr after the majority of the HIRES and HARPS data were taken. On some nights, we observed AD Leo multiple times to better sample the short period of 2.23 days. We call this subset of data "VIS1" and "NIR1" given that AD Leo was observed again later in 2020 as part of a DDT[13] program, for which 20 data points were obtained over ∼3 days, which we call subset "VIS2" and "NIR2". The RVs and several activity indicators (e.g., CRX – chromatic index, dLW – differential line width) from both subsets were first extracted with `serval` (Zechmeister et al. 2018), so that they are corrected for barycentric motion, secular acceleration, and instrumental drift. The final RVs we use had nightly zero-points applied (Tal-Or et al. 2019; Trifonov et al. 2020). Figure 4 displays the CARMENES data and the best respective models (detailed in Sect. 6). For calculating the CCF parameters within CARMENES, weighted binary masks, which depend on spectral type and $v \sin i$, are produced by coadding spectra corrected for tellurics & RV shifts and then selecting pronounced minima (Lafarga et al. 2020). From there, the CCF parameters, namely, the bisector span (BIS), contrast, and full-width half-maximum (FWHM), are obtained for both the VIS and NIR channel.

3.2. Archival RV data

HARPS-South. Spectroscopic data for AD Leo are in the public archive from the High-Accuracy Radial velocity Planet Searcher (HARPS, Mayor et al. 2003), a high-resolution échelle spectrograph located at the ESO 3.6 m telescope at La Silla Observatory in Chile. We retrieved a total of 52 spectra that were taken over a span of ∼4500 days. Due to a fiber-upgrade intervention (Lo Curto et al. 2015), we considered the HARPS data as coming from two separate instruments, before and after this upgrade. After the intervention, only five data points were taken close to one another (within 2 days) and much later than the earlier data. These data also have a very low root-mean-square (RMS) deviation from their mean. We did not consider them for the further analysis since they could fit anywhere in a model with a large offset and therefore do not provide new insight. Thus, for the rest of the analysis, we used the 47 HARPS spectra from before the intervention. Additionally, the majority of data (i.e., 33 points) were taken over the course of ∼115 days (January–May 2006). The spectra were first processed using `serval` (Zechmeister et al. 2018) to obtain the RVs and helpful stellar activity indicators (e.g., CRX, dLW, Hα, see Zechmeister et al. 2018, for more explanation). Nightly zero-points corrections provided by Trifonov et al. (2020) were applied to the RVs[14] and are used in our analysis (Table A.4).

HIRES. We collected 43 spectra from the high-resolution spectrograph HIRES (Vogt et al. 1994) mounted on the 10 m Keck-I telescope located at the Mauna Kea Observatory in Hawai'i, which has been in service since 1994. The data were taken over the course of 4500 days. A majority of them (i.e., 22 points) were taken in 2005/2006 over 120 days and, moreover, overlap with the higher cadence HARPS data (see Fig. 2). Butler et al. (2017) released a large RV database of 64 480 observations for a sample of 1699 stars, which was later reanalyzed

[13] Director's Discretionary Time.

[14] https://www2.mpia-hd.mpg.de/homes/trifonov/HARPS_RVBank.html

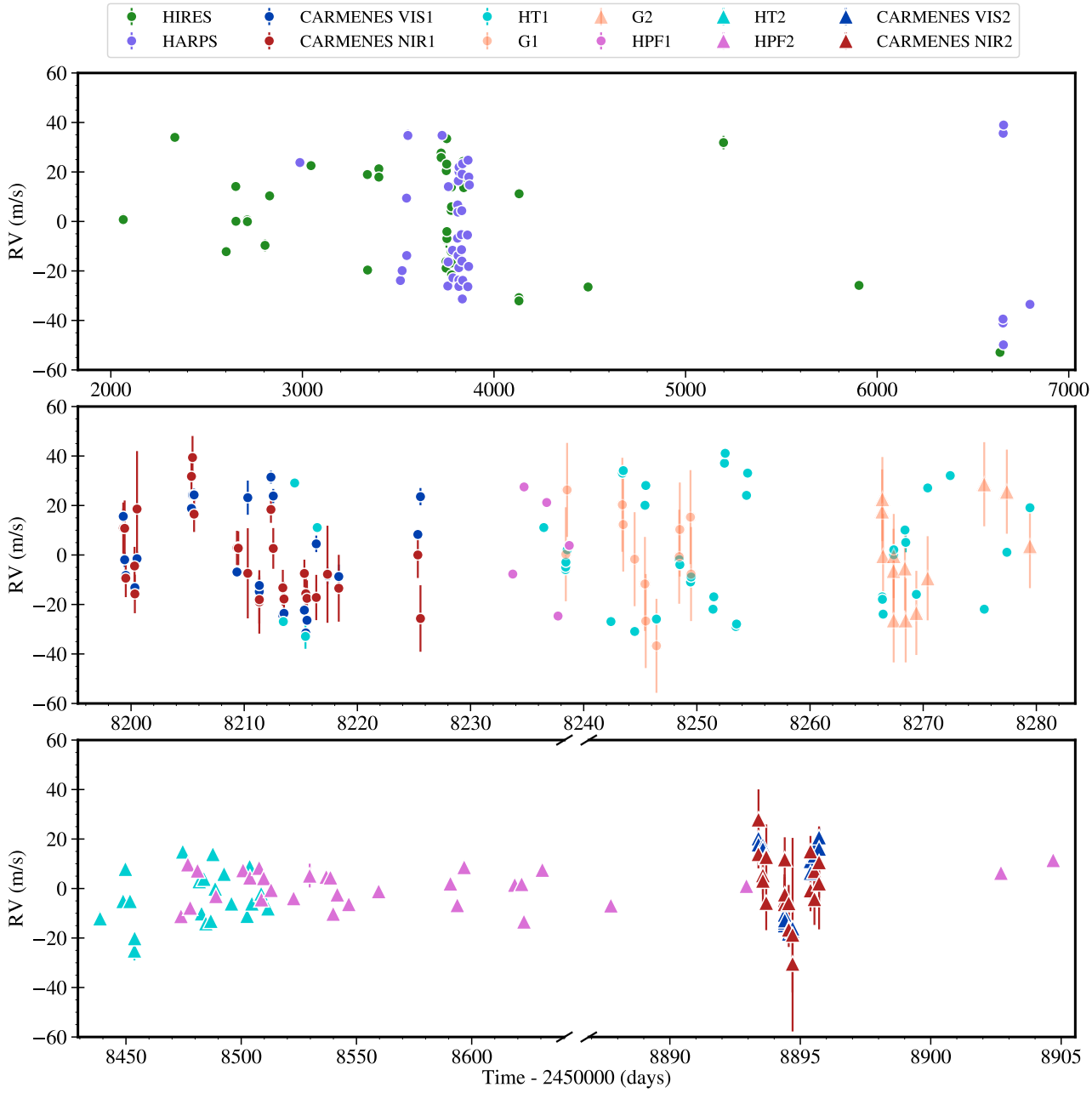

Fig. 2. Time series of all RVs with instrumental offsets accounted for. The RV uncertainties are included, though many are too small to be seen in the plots. The HIRES and HARPS data span a large time range and the rest of the data come in ∼12 yr later after the time when the majority of the previous data were taken. The time axis is interrupted in several places, and stretched differently between the individual sections. Additionally, the majority of HIRES and HARPS time series are overlapping each other. Four of the HARPS-N data overlap with CARMENES data; and the GIANO-B data are taken all within the first observing run for HARPS-N. The first season of HPF data overlaps with the HARPS-N and GIANO-B data sets whereas the HPF second season overlaps with the HARPS-N and CARMENES second season.

by Tal-Or et al. (2019) for minor, though significant systematic effects, such as an RV offset due to the CCD upgrade in 2004, long-term drifts, and slight intra-night drifts. Therefore, we continued with the corrected HIRES RVs provided by Tal-Or et al. (2019), presented in Table A.5. Data from HIRES are also specifically addressed further under Sect. 5.2.

3.3. Additional RV data from the literature

Radial velocities are taken directly from C20 and R20, as described in the following paragraphs, and are used for the analysis as well.

GIARPS. We include spectroscopic data taken in GIARPS mode (Claudi et al. 2017), where high resolution spectroscopic measurements are obtained simultaneously with HARPS-N (Cosentino et al. 2012, extracted with the TERRA pipeline) and with GIANO-B (Oliva et al. 2006) reduced with the on-line DRS pipeline and the off-line `GOFIO` pipeline. Both instruments are located at the 3.58 m Telescopio Nazionale *Galileo* (TNG) at the Roque de los Muchachos Observatory in La Palma, Spain. The GIARPS mode is similar to CARMENES in the sense it also addresses potential variations of a signal amplitude over a wide wavelength range. There were two runs of HARPS-N, with only the first run having simultaneous GIANO-B data; four

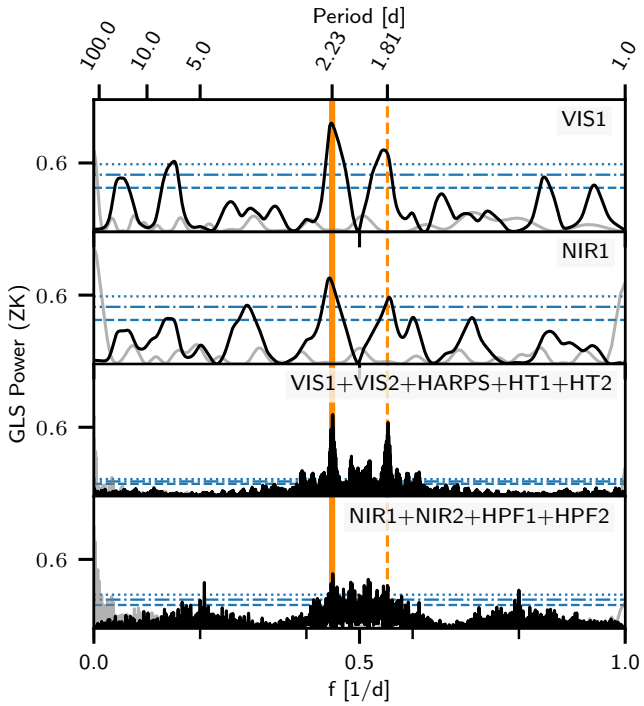

Fig. 3. GLS periodograms (black) and window functions (gray) for the CARMENES VIS1 and NIR1 RV data sets, as well as for the combined optical (i.e., VIS1, VIS2, HARPS, HT1, and HT2) and near-infrared (i.e., NIR1, NIR2, HPF1, HPF2) instruments, with offsets accounted for. The horizontal lines correspond to FAP levels of 10% (dashed), 1% (dash-dotted), and 0.1% (dotted). These are computed by using the randomization technique for 10 000 samples. The orange solid line corresponds to the rotational period of 2.23 days, whereas the orange dashed line represents the 1.81 d alias signal due to daily sampling.

of the HARPS-N data overlap with the CARMENES data. To stay consistent with C20, we also consider two separate runs for HARPS-N and GIANO-B, and designate them as "HT1", "HT2", "G1", and "G2" for our analysis. Due to the high uncertainty on the data points from the GIANO-B instrument, we do not include them for our analysis.

HPF. Our last data set comes from the Habitable-zone Planet Finder (HPF), a stable NIR Doppler spectrograph that is designed to reach 1–3 m s^{-1} RV precision for M dwarfs with the help of wavelength calibration via a custom NIR laser frequency comb (Mahadevan et al. 2012, 2014). The spectrograph is installed at the 10 m Hobby-Eberly Telescope at McDonald Observatory in Texas. The HPF data are of high quality providing an RV precision of 1.5 m s^{-1} on AD Leo. A total of 35 HPF RVs were obtained, five of which during HPF commissioning and 30 afterwards, namely "HPF1" and "HPF2". The HPF data in this paper are tabulated in R20. These data overlap with optical RV data from HARPS-N and show also an amplitude decrease between observing seasons.

4. Wavelength dependence of RV signal in CARMENES data

Signals in RV measurements induced by dark spots corotating on the stellar surface are expected to be more pronounced in the bluer wavelength regime for M-dwarf stars (e.g., Desort et al. 2007; Reiners et al. 2010; Mahmud et al. 2011; Sarkis et al. 2018). In contrast, a true planetary signal should have an amplitude and phase that are consistent both in time and as a function of wavelength.

4.1. Chromatic index

The chromatic index is a photospheric activity indicator that measures the RV-log λ correlation where a straight line is fit to the RV values computed from individual échelle orders as a function of log λ (Zechmeister et al. 2018; Tal-Or et al. 2018). This acts as a measure of wavelength dependence as caused by cool spots on the surface of M dwarfs. However, without further modeling, it does not provide any insight as to how large the spot coverage fraction is or what the star-spot temperature contrast may be. The RV-CRX correlations are shown for CARMENES VIS, CARMENES NIR, and HARPS, in Figs. C.1, C.2, and C.3, respectively. The CARMENES VIS data show a clear anticorrelation ($r = -0.82$) indicating chromatic dependency and HARPS surprisingly demonstrates a strong, positive correlation ($r = +0.80$), whereas the CARMENES NIR data present a moderate, negative correlation ($r = -0.30$).

Different slopes at different wavelengths are not necessarily unexpected. In principle, this depends on which mechanism is dominating, namely either the star-spot temperature contrast or Zeeman broadening, where a more negative RV-CRX correlation suggests the former to be predominant. This is also equivalent to the amplitude of the RVs due to stellar features decreasing with longer wavelengths (Sect. 4.2). The fact that the slopes of CARMENES and HARPS are in contradiction could simply indicate that different mechanisms are prevalent. Likewise, taking into consideration that we are probing very different spectral lines at different wavelengths may introduce a trend with wavelength that is not yet well understood. When considering only the orders of CARMENES VIS that overlap with the HARPS wavelength range, the correlation would still stay the same. Here, the wavelength range considered is now equivalent, nonetheless the signs of the slopes are inconsistent. No firm conclusion can be drawn, though this could be a result of different mechanisms dominating during different time periods of long-term stellar activity.

Furthermore, the correlation plot for the CARMENES VIS demonstrates a "closed-loop" (circular) behavior (see Sect. 7.2.5 for a discussion). Removing the CRX trend on just the CARMENES data results in two-fold decrease in the rms of the corrected RVs (from 18.5 m s^{-1} to 9.2 m s^{-1} for first season and from 15.6 m s^{-1} to 9.3 m s^{-1} for the second). This subtraction was not performed on the CARMENES NIR data since the Pearson-r coefficient was not large enough (Jeffers et al. 2022).

4.2. Wavelength segments

The CARMENES VIS channel records 55 échelle orders, 42 of which are considered when computing the RV measurement via a weighted mean (Zechmeister et al. 2018). We chose to combine these orders into four wavelength segments where each segment consists of ten (or 11) échelle orders in order to preserve some precision, and the RVs are then recomputed for each respective wavelength coverage. Similarly, the CARMENES NIR channel has 28 RV orders over the Y, J, and H photometric bands. Due to telluric contamination, especially in the J band (Reiners et al. 2018), only a selected few orders are considered (Bauer et al. 2020). We then use two wavelength segments, one for the Y and another for the H band, consisting of 12 and seven individual orders, respectively. For this wavelength segment analysis, we

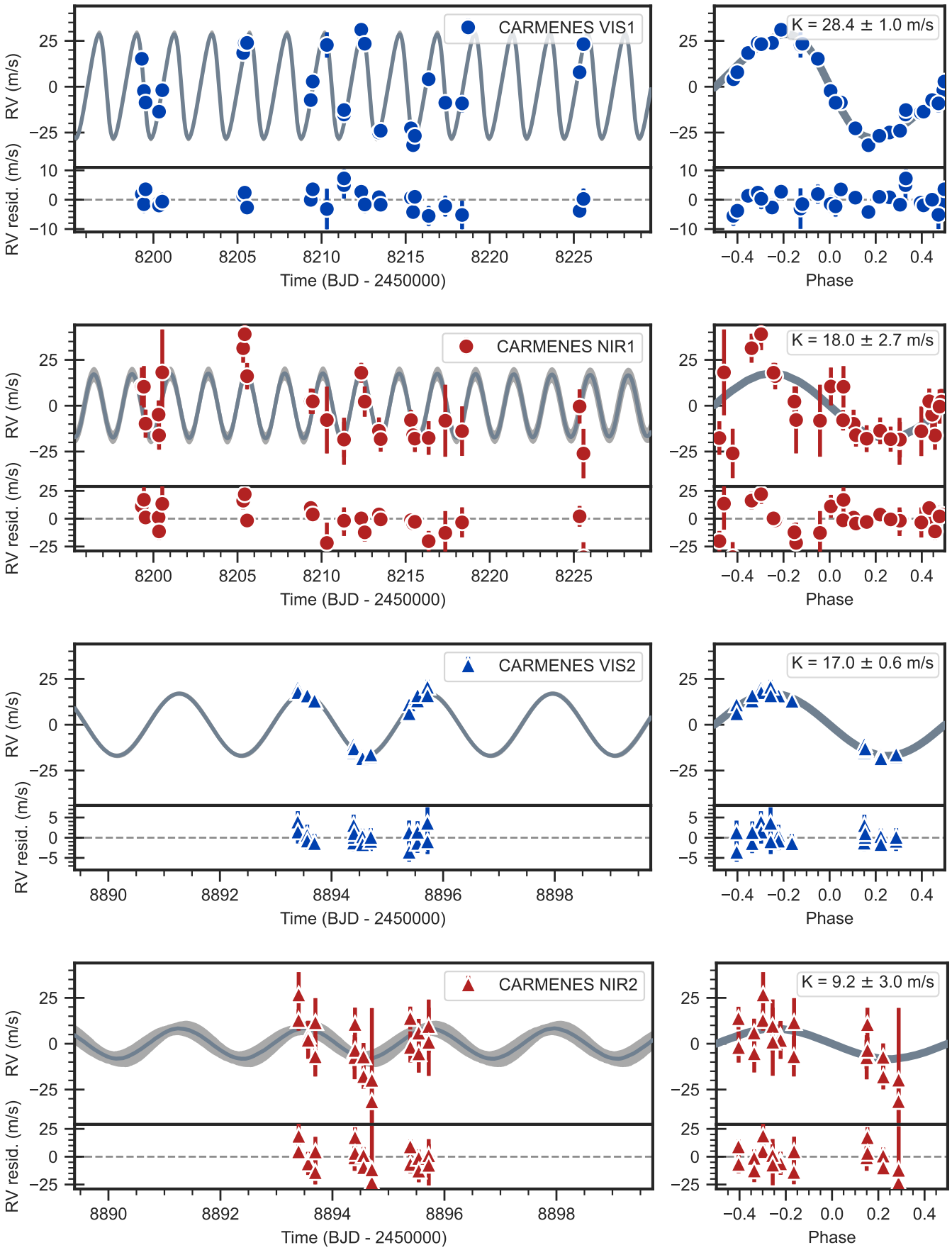

Fig. 4. Radial-velocity times series and phase-folded plots for the CARMENES VIS1, NIR1, VIS2, and NIR2 data (*top to bottom*) with residuals from the best-fit model. In some cases, especially in the panels with the VIS1 and VIS2 data, the uncertainties are too small to be seen in the plots. The best-fit models are overplotted (gray line) along with the 68% posterior bands (gray shaded regions).

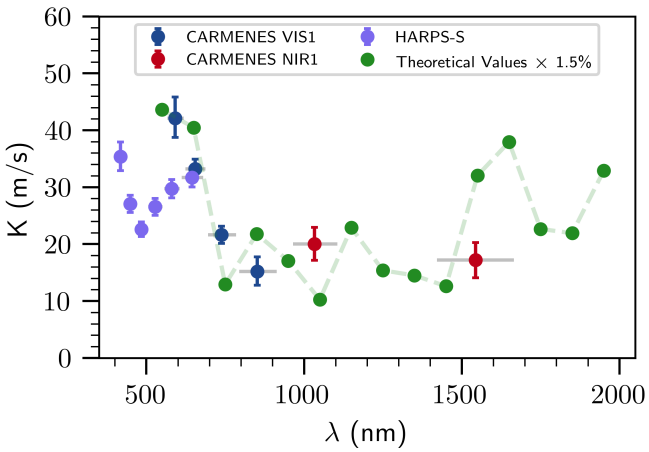

Fig. 5. Radial-velocity semi-amplitudes as a function of wavelength for the wavelength chunks from HARPS and the CARMENES VIS and NIR spectographs. The gray horizontal lines for each data point correspond to the wavelength coverage considered when recomputing the RV for the wavelength chunk. The green dots connected by a dashed line represent the theoretical values of a 1.5% spot coverage on a 3700 K, $v \sin i$ of 5 km s^{-1} star with a temperature difference of 200 K taken from Reiners et al. (2010). The theoretical values are binned in 2 to serve as a better comparison to the wavelength bins provided by the real data.

consider just the season one CARMENES data because the data from season two exhibit an amplitude decrease (see Sect. 6.3), and likewise, breaking up the orders would introduce noise given the few data points over a short time span.

Each wavelength segment is treated as an individual data set. We fit a simple sinusoid to obtain K, the semi-amplitude of the signal and 1σ errors. When doing this, the semi-amplitude clearly decreases with increasing wavelength in the optical regime, but then reaches a plateau when continuing in the near-IR (Fig. 5). This behavior of decreasing but then constant RV semi-amplitude is in agreement with Reiners et al. (2010) for a dark spot on the surface of an M dwarf; specifically, a spot covering 1.5% of the projected surface, with a temperature 200 K cooler than the star (assumed $T_{\rm eff}$ = 3700 K), and a stellar $v \sin i$ of 5 km s^{-1}, in line with AD Leo's stellar parameters[15] (Table 1). Simulations show a linear relation between spot coverage and RV semi-amplitude for low spot coverage values. A large spot-star temperature difference ($T_{\rm spot} = \frac{2}{3} T_{\rm eff}$), in comparison, would not cause a notable semi-amplitude dependency as a function of wavelength; however, it is not likely for cooler stars, such as AD Leo, to have large spot-star temperature differences (Bauer et al. 2018).

Likewise, the HARPS instrument covers 72 spectral orders, of which 61 produce reliable RVs after being processed by `serval` (signal-to-noise is too low for the others). Similarly, we computed six wavelength chunks with ten spectral orders each (11 for the reddest chunk) and followed the same methodology as for the CARMENES wavelength chunks. Reiners et al. (2013) and T18 performed similar analyses but differed in interpretation. T18 suggested there is no dependence on wavelength, whereas Reiners et al. (2013) claimed otherwise and mentioned that this is the first case of a known active star with increasing amplitude with wavelength. Here, we find a slight positive incline, which is plotted for comparison to the CARMENES data in Fig. 5. The positive slope can be interpreted as being due to the Zeeman effect, which has the opposite effect compared to a spot-temperature difference where the RV amplitude is predicted to increase for redder wavelengths (Reiners et al. 2013). For the overlapping wavelengths, the amplitudes of the wavelength chunks do not particularly agree which can simply be an artifact that HARPS data were taken at a time where AD Leo exhibited less activity in the RVs, as is likewise present behavior in the photometry (Sect. 2.2).

[15] We adopt the higher value of $v \sin i$ (i.e., 5 km s^{-1}) rather than 2 km s^{-1} (as also computed in Reiners et al. 2010) because AD Leo is relatively active for its $v \sin i$.

5. Identifying individual spectral lines affected by stellar activity

We further investigate the possible effect of stellar activity on the spectral lines themselves. We follow an approach similar to Dumusque (2018), which has proven to be fruitful for a selection of G-K dwarfs whose RVs are dominated by activity. Essentially, we use the CCF technique, where we obtain a binary mask that contains all available, reliable lines for a spectrum (following Lafarga et al. 2020). We then compute individual RVs of the few thousands of spectral lines we have identified, and obtain an RV time series for each line. To classify the lines according to their sensitivity to activity, we correlate their RVs to an activity indicator obtained from the same spectra (such as the CRX, BIS, or the total RV). We then select a subsample of spectral lines that are least affected by stellar activity (those that do not show a strong correlation) and recompute the RVs using this subsample to mitigate stellar activity. The recomputed RVs then have a smaller scatter and the modulation due to stellar rotation decreases.

This technique has been tested for other M dwarfs similar to AD Leo (i.e., spectral types 3.0–4.5 V, relatively low rotational velocities and high activity levels) that are well-known to exhibit strong stellar activity signals (e.g., YZ CMi, EV Lac) and appears to perform well and as expected (Lafarga, priv. comm.). We found similar results regardless of the activity indicator (total RV, CRX or BIS) used to compute the correlations with the individual line RVs, with the total RV yielding slightly smaller RV scatters.

5.1. Individual spectral lines using the CARMENES data

Specifically for AD Leo, we compare the computed individual line RVs to the CRX or the BIS and estimate the strength of stellar activity based on these correlations. We focus on just the first season in 2018, namely, VIS1, since the second season only covers a bit more than one rotation cycle and this then introduces too much scatter due to the photon noise being too high. To quantify the correlation strength, we used the Pearson correlation coefficient r. We considered lines as 'inactive' with r close to 0. We also discarded lines that had time series scatter larger than 400 m s^{-1}, as measured from their weighted standard deviation (WSTD) RV; these are weak lines that mostly add noise to the recomputed RVs. Our results for the correlation with the CRX are shown in Fig. 6, where we generated three line subsamples: (1) all spectral lines – black, (2) where $|r| \leq 0.30$ – orange Regarding the modulation, the periodograms of these two data sets show a decrease in the power of the 2.23 days peak compared to the all-lines data set, but there is still some power left (false alarm probability (FAP) > 10% and almost 10% for the orange and blue subsets respectively).

This would be clear if the RV scatter decreased for the orange or blue data sets. However, since we do not observe such

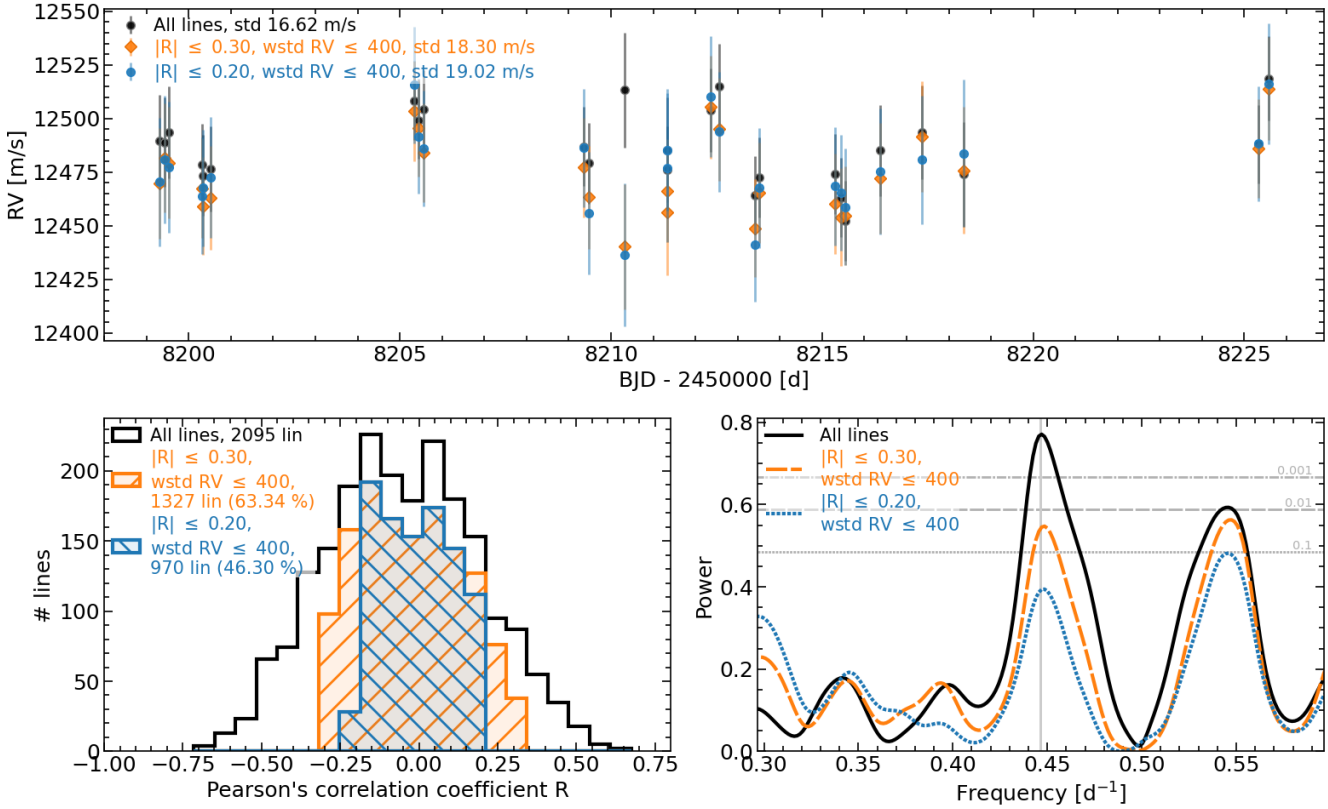

Fig. 6. Three various subsamples of the spectral lines: black – all, orange – $|r| \leq 0.30$, and blue – $|r| \leq 0.20$. *Top:* absolute RVs versus time for the first CARMENES VIS season. *Bottom left:* histogram of the Pearson-r correlation coefficient when comparing the RVs from individual lines to the CRX. The criteria for the subsamples are illustrated here. *Bottom right:* zoomed-in GLS periodograms around the signal of interest of the RVs of the subsamples. The orange subsample still shows power at 2.23 days, whereas the blue subsample still has a nonsignificant bump but it is noise limited.

a decrease, it is difficult to discern what is causing the periodogram behavior. The increase in the RV scatter could be caused by increasing photon noise in the RVs of the orange and blue data sets (because we are using a smaller number of lines to compute the RVs, hence less signal). Then, the decrease in the periodogram power could be due to this increasing noise, and not to a decrease in the activity signal.

Compared to the results from other stars (e.g., EV Lac, YZ CMi), the correlations found for AD Leo are much weaker (the mean correlation coefficient r is ∼–0.2 and some of them show $|r| \geq 0.8$ for the correlation with the CRX, while for AD Leo, the mean is at 0 and very few lines have $|r| \geq 0.6$). This lack of clear correlations indicates that the correlations that we find for AD Leo do not have much information related to the activity of the star, and this could be why we are not able to effectively mitigate the stellar activity signal in the RVs.

This difference in the correlation strength could be due to the different RV amplitudes of the stars. AD Leo shows a small RV amplitude compared to the other considered stars: $K \sim 25\,\mathrm{m\,s^{-1}}$ in comparison to EV Lac with $\sim 100\,\mathrm{m\,s^{-1}}$. Both stars have similar spectral types and activity levels (for EV Lac, pEW(Hα) = -4.983 ± 0.021, as computed from the CARMENES observations, Schöfer et al. 2019), so the difference in RV amplitudes seems to be caused by different spot configurations. AD Leo has a relatively low inclination ($i \sim 13°$) in comparison to EV Lac or the other considered stars (≥60°, see e.g., Morin et al. 2008). This close to pole-on inclination could cause any visible corotating spots to induce a smaller modulation in the RVs simply because $v \sin i$ is smaller. Also, the photosphere of AD Leo could be more homogeneously spotted, also inducing smaller RV modulations.

To summarize, we recomputed the RVs using only the lines least affected by activity in the AD Leo spectra, and observed a decrease in the periodogram peak at 2.23 days (0.1–10%); however, there was still some significant residual power and we did not observe a significant decrease in the RV scatter. This could be due to AD Leo having a different activity signal in the RVs than other stars with similar characteristics, for which we observe a clear mitigation of activity.

5.2. Other spectroscopic activity indicators

To aid in disentangling the origin of a signal, a variety of stellar activity indicators, such as photometric variability, bisector inverse slope (BIS, the measurement of asymmetry of the CCF), Ca II infrared triplet (IRT), Hα, CRX, the dLW, or the TiO bands, has been shown to be successful in identifying and indicating a nonplanetary signal. In the literature, periodic RV signals are often considered planetary in nature if the same signal is not found in activity indicators. Therefore, it is important to examine as many activity indicators as possible.

Correlations between the mentioned stellar activity indicators (when available) and the RVs along with the GLS periodograms for these indicators can be found in Appendix C for both the CARMENES VIS and NIR channel as well as for the HARPS instrument. The strong correlations found with the CRX was already discussed in Sect. 4.1. The BIS-RV anticorrelation for the VIS channel ($r = -0.79$) is inline with the same

anticorrelation found by C20 in the HARPS-N data ($r = -0.74$). Additionally, we look at the dLW However, in our case, there seems to be no correlation. Along with the dLW, other expected stellar activity indicators such as the emission of Hα (Kürster et al. 2003; Hatzes et al. 2015; Hatzes 2016; Jeffers et al. 2018; Barnes et al. 2014) and the Ca II IRT (Gomes da Silva et al. 2011; Martin et al. 2017; Robertson et al. 2015, 2016) seem to not show peaks at 2.23 days in periodograms and exhibit no strong or moderate correlations. These findings are in agreement with Lafarga et al. (2021) for a high-mass and Hα-active star as AD Leo. In addition, we also consider the pseudo-equivalent widths (pEW') of various potential stellar activity lines as described in Schöfer et al. (2019), though find no correlations or significant peaks other than suggestive bumps at 1.8 days (i.e., the daily alias of 2.23 days).

6. Modeling the time dependence of the RV signal

Discontinuous sampling over the course of a long time baseline impedes obtaining key information as to what occurs in large data gaps – as is the case between the majority of the HIRES, HARPS data and CARMENES, GIARPS, HPF data for AD Leo being 12 yr apart. Remarkably, the 2.23 days signal persisted over all this time, however, it is evident that amplitude changes and phaseshifts occurred. Therefore, given such a rich RV data set, we test out the current approaches for modeling stellar activity on a real-life example and present our results below.

6.1. Model setup

We model the RV data using two components: a stable component (in amplitude, period, and phase) and a variable component. The former is described by a deterministic model, typically a circular or eccentric Keplerian orbit. We would like to emphasize that when we use a Keplerian model, we consider it more as a "stable model" which may include both a planetary companion and a stable aspect of stellar activity, or only one of the two. Therefore, parameters that are typically called $P_{\rm planet}$ and $K_{\rm planet}$ to represent the period and semi-amplitude of the Keplerian signal are rather referred as $P_{\rm stable}$ and $K_{\rm stable}$ to indicate that we are considering a "stable mode" that appears persistent. From here on, we use the terms Keplerian model and stable model interchangeably, though we are not claiming that this component is solely due to a planetary companion. As for the variable component, typically comprising the quasi-periodic behavior of stellar activity, we do not currently possess a deterministic model, therefore, we use a nonparametric GP model to describe these modulations. We employ two different kernels.

The first is an exponential-squared-sine-squared kernel, that is, quasi-periodic (QP-GP) kernel, provided by `george` (Ambikasaran et al. 2015),

$$k_{i,j}(\tau) = \sigma_{\rm GP}^2 \exp\left[-\alpha_{\rm GP}\tau^2 - \Gamma_{\rm GP}\sin^2\left(\frac{\pi\tau}{P_{\rm GP,\,rot}}\right)\right] \quad (1)$$

where $\tau = |t_i - t_j|$ is temporal distance between two points, $\sigma_{\rm GP}$ is the amplitude of the GP modulation, $\alpha_{\rm GP}$ is the inverse length-scale[16] of the GP exponential component, $P_{\rm GP,\,rot}$ corresponds to the recurrence timescale, and $\Gamma_{\rm GP}$ is the smoothing parameter. The former term is an exponential that can model the decorrelation due to the changes in phase and amplitude as active regions grow and decay over time, whereas the latter term accounts for the reoccuring periodicity.

The second kernel is a sum of two stochastically driven, damped harmonic oscillator (SHO) terms, or a double SHO GP (dSHO-GP), where the power spectrum of one SHO term is given by Anderson et al. (1990),

$$\mathrm{SHO}_1(\omega_{\rm GP}) = \sqrt{\frac{2}{\pi}}\frac{S_0\omega_1^4}{(\omega_{\rm GP}^2-\omega_1^2)^2+\omega_1^2\omega_{\rm GP}^2/Q_1^2} \quad (2a)$$

and

$$\mathrm{SHO}_2(\omega_{\rm GP}) = \sqrt{\frac{2}{\pi}}\frac{S_0\omega_2^4}{(\omega_{\rm GP}^2-\omega_2^2)^2+\omega_2^2\omega_{\rm GP}^2/Q_2^2}, \quad (2b)$$

for which we applied a reparametrization using the hyperparameters

$$Q_1 = 0.5 + Q_0 + \delta Q \quad (2c)$$

$$\omega_1 = \frac{4\pi Q_1}{P_{\rm GP,\,rot}\sqrt{4Q_1^2-1}} \quad (2d)$$

$$S_1 = \frac{\sigma_{\rm GP}^2}{(1+f)\omega_1 Q_1} \quad (2e)$$

$$Q_2 = 0.5 + Q_0 \quad (2f)$$

$$\omega_2 = 2\omega_1 = \frac{8\pi Q_1}{P_{\rm GP,\,rot}\sqrt{4Q_1^2-1}} \quad (2g)$$

$$S_2 = \frac{f\sigma_{\rm GP}^2}{(1+f)\omega_2 Q_2}, \quad (2h)$$

and where $\sigma_{\rm GP}$ is again the amplitude of the GP kernel, $P_{\rm GP,\,rot}$ is the primary period of the variability, Q_0 is the quality factor for the secondary oscillation, δQ is the difference between the quality factors of the first and second oscillations, and f represents the fractional amplitude of the secondary oscillation with respect to the primary one.

We investigate multiple models to see which one is preferred for each individual data set as well as for the combined data set comprising all available RVs. The models being tested are:

1. Keplerian-only models, i.e., both circular and eccentric,
2. GP-only model, either with a QP-GP or a dSHO-GP, as a proxy to describe the quasi-periodic nature of the stellar activity,
3. Mixed (Keplerian + GP) models, to describe stable components with variable ones.

We use the model-fitting python package, `juliet` (Espinoza et al. 2019) in order to compare these models using a Bayesian framework. For our purposes, the RVs are modeled by `radvel`[17] (Fulton et al. 2018), and the GP models with the help of `george`[18] (Ambikasaran et al. 2015) and `celerite`[19] (Foreman-Mackey et al. 2017), where we use the `dynesty`[20] package (Speagle & Barbary 2018; Speagle 2020) to execute the Nested Sampling algorithm in order to efficiently compute the Bayesian model log evidence, $\ln\mathcal{Z}$. The main motivation for calculating the Bayesian log evidence ($\ln\mathcal{Z}$) is to perform model comparisons. Outlined by Trotta (2008), we follow the rule of

[16] The parameter $\alpha_{\rm GP}$ is defined as $1/l^2$, where l is the timescale of variations. The original relation in Espinoza et al. (2019) incorrectly defined $\alpha = 1/2l^2$. This has since been corrected.

[17] https://radvel.readthedocs.io/en/latest/

[18] https://george.readthedocs.io/en/latest/

[19] https://celerite.readthedocs.io/en/stable/

[20] https://github.com/joshspeagle/dynesty

thumb that a $\Delta \ln \mathcal{Z}$ greater than 5 between two models indicates strong evidence in favor for the model with the larger Bayesian log evidence (odds are ~150–1), whereas a $\Delta \ln \mathcal{Z}$ more than 2.5 indicates moderate evidence for the winning model, and anything less we consider to be inconclusive.

6.2. Prior setup

The RV periodograms (Fig. 3) indicate the interesting signal to be around 2.23 days. Thus, for all models with a Keplerian, the prior of the period of the stable component, $P_{\rm stable}$, was kept uniform, but relatively narrow, $\mathcal{U}$(2.0 days, 2.5 days), in order to avoid picking up aliases (i.e., 1.8 days due to the daily sampling), and similarly for the time of transit center[21], t_0, $\mathcal{U}$(2458200 days, 2458202 days), in order to cover solely one cycle and to avoid picking up other potential modes. The semi-amplitude prior was simply uniform as well, $\mathcal{U}(0\,{\rm m\,s^{-1}}, 50\,{\rm m\,s^{-1}})$.

As for the GP models, the rotational period, $P_{\rm GP,\,rot}$ follows the same prior as $P_{\rm stable}$ for consistency. Then, we consider wide log-uniform priors for the other QP-GP hyperparameters: $\Gamma_{\rm GP}$ (between 10^{-2} and 10^{2}) and $\alpha_{\rm GP}$ (between 10^{-10} day^{-2} and 10^{-1} day^{-2}, corresponding to timescales of ~3 to ~70 000 days). For the dSHO-GP hyperparameters: Q_0 was log-uniform (from 10^2 to 10^5), as well as δQ (from 10^{-1} to 10^5), and f was kept uniform (between 0 and 1). For both GP kernels, the sigma of the GP was kept log-uniform (between 0.1 and 70 m s^{-1}) where each instrument had its own, noted as $\sigma_{\rm GP,\,inst}$, because each instrument has its own characteristics, such as noise level, zero point offset, wavelength range, or intrinsic stellar jitter. The other GP hyperparameters are shared. Additional instrumental jitter terms (log-uniform from 10^{-2} to 30 m s^{-1}) and offsets for each individual instrument were considered as well.

6.3. Results

We applied this recipe to the three following data sets: CARMENES VIS only, CARMENES NIR only, and the entire RV data set. The resulting posteriors on the $P_{\rm stable}$ ($P_{\rm GP,\,rot}$ if using a GP), semi-amplitude $K_{\rm stable}$ ($\sigma_{\rm GP,\,inst}$ if GP), added instrumental jitter terms ($\sigma_{\rm inst}$) and eccentricity along with the differences in Bayesian log evidence can be found in Table 3.

6.3.1. CARMENES only

Focusing on just the CARMENES season one data, an eccentric ($e \sim 0.19$) Keplerian model is preferred over a circular model for the VIS channel ($\Delta \ln \mathcal{Z} \sim 5$). This is in agreement with the optical HARPS-N data where C20 also found a similar eccentricity when applying a Keplerian-only model. As for the NIR channel, a circular model performs best. Moreover, the NIR data does not actually have a clear model preference, simply attributed to the lower precision. The amplitude decreased from $28.43^{+0.94}_{-0.98}$ m s^{-1} in the VIS1 data to $18.0^{+2.6}_{-2.7}$ m s^{-1} in the NIR1 data. When introducing combined stable plus GP models, the stable component dominates and the GP component is not needed, in other words, $\sigma_{\rm GP}$ becomes consistent with zero. This finding is anticipated given that the time span of the data is roughly ~10 cycles of the periodicity, which would be too short for any noticeable changes of the stellar spot pattern assuming a long spot lifetime.

[21] The time-of-transit center is used within the `juliet` framework in regards to the phase of the orbit.

For the season two data, we slightly readjusted the priors as introduced in Sect. 6.2. The time of transit center was moved to $\mathcal{U}$(2458893 days, 2458895 days) to comply with the pertinent time stamps. Likewise, the period was narrowly constrained, $\mathcal{U}$(2.22 days, 2.24 days), to ensure the correct periodicity is recognized given the short time baseline of less than two periodic cycles. Likewise for this reason, just the circular Keplerian-only models were performed, and as a result, the posterior values are not included in Table 3. Similarly to the season one data, there was also an amplitude decrease between the instruments, namely from $17.02^{+0.63}_{-0.62}$ m s^{-1} to $9.2^{+3.0}_{-2.6}$ m s^{-1} between VIS2 and NIR2, respectively, both of which are lower with respect to their season one counterparts. Figure 4 shows how the time series and phase-folded plots using the best model fits for the four CARMENES data sets appear reasonable, showing a uniformly distributed scatter in the model residuals. We additionally tested out combining the two seasons with each respective instrument (i.e., VIS1+VIS2, NIR1+NIR2) and applied all the models (including those with GPs), finding that the circular Keplerian was favored for both.

6.3.2. Whole data set

Next, we considered the whole AD Leo RV data set. We expect the Keplerian-only models, where the amplitude for all given instruments is shared, to perform poorly given that the amplitude is clearly decreasing as a function of wavelength (shown in Sect. 4). The idea of combining all available data sets covering a wide wavelength range is that the data set with the smallest amplitude, specifically the NIR data, will act as an upper limit for any stable signal, whereas the GP component will adapt the difference. Within the framework of `juliet`, the data is first attempted to fit the deterministic model as best as possible, where the GP is then applied to the residuals. Likewise, we expect that the added jitter terms and GP amplitude parameters for the redder instruments will be consistent with zero in the mixed model because the stable model will most likely saturate for the redder instruments. The role of the GP is to account for the excess amplitude observed with the bluer instruments.

The preferred model among all is the mixed circular Keplerian + dSHO-GP model. When compared to a Keplerian-only model, it exceeds in Bayesian log evidence tremendously ($\Delta \ln \mathcal{Z} \sim 180$), but it does not prevail against a dSHO-GP-only model that enormously ($\Delta \ln \mathcal{Z} \sim 3.5$). As anticipated, the Keplerian-only models fail to explain the data in the sense that finding a common amplitude is not feasible such that the jitter values become too high, and likewise, the phase shifts are quite strong that a simple sinusoid cannot describe this behavior. Surprisingly, even though the dSHO-GP-only model is flexible and could model the data well, the evidence suggests that a model containing an additional stable periodic component is favored. Likewise, the same concept applies for the models including the QP-GP kernel, though including the additional stable component produced a $\Delta \ln \mathcal{Z} \sim 10$ rather than ~3.5 for the dSHO-GP models, that is, very strong evidence for one model versus bordering just moderate evidence. This delicate boundary could change the interpretation. Tests on simulated RV data based on StarSim (Herrero et al. 2016) indicate that a Keplerian signal is in rare cases more efficient than the QP-GP in modeling a coherent activity signal (Stock et al. 2022).

We find that the stable signal amplitude $K_{\rm stable}$ is 16.6 ± 2.2 m s^{-1}, where both the $P_{\rm stable}$ and $P_{\rm GP}$ is rounded to 2.23 days. All posteriors for the different models can be found in Table 3

Table 3. Model comparison of RV fits done with `juliet` comparing a Keplerian model, a red-noise model, and a mixture of both for the various instrument data sets: CARMENES VIS1, CARMENES NIR1, and the combined data set.

			QP-GP			dSHO-GP		
	circ.	ecc.	GP	circ. + GP	ecc. + GP	GP	circ. + GP	ecc. + GP
CARMENES VIS1								
$P_{\rm stable}$	$2.2362^{+0.0054}_{-0.0056}$	$2.2344^{+0.0029}_{-0.0030}$	...	$2.238^{+0.150}_{-0.014}$	$2.2346^{+0.0033}_{-0.0035}$	...	$2.237^{+0.015}_{-0.008}$	$2.2348^{+0.0036}_{-0.0036}$
$K_{\rm stable}$	$25.9^{+1.4}_{-1.5}$	$28.43^{+0.94}_{-0.98}$	...	19^{+11}_{-16}	$28.4^{+1.1}_{-1.2}$	...	$22.6^{+7.2}_{-16.0}$	$28.3^{+1.2}_{-1.5}$
$P_{\rm GP}$	...	...	$2.2332^{+0.0035}_{-0.0038}$	$2.226^{+0.011}_{-0.019}$	$2.28^{+0.16}_{-0.19}$	$2.2329^{+0.0048}_{-0.0049}$	$2.224^{+0.013}_{-0.017}$	$2.24^{+0.19}_{-0.14}$
ecc.	0.0 (fixed)	$0.192^{+0.030}_{-0.031}$	...	0.0 (fixed)	$0.186^{+0.032}_{-0.033}$	...	0.0 (fixed)	$0.187^{+0.034}_{-0.038}$
$\sigma_{\rm GP,\ CARMENES\ VIS1}$	...	...	38^{+18}_{-14}	23^{+24}_{-15}	$1.8^{+7.6}_{-1.7}$	$18.3^{+8.2}_{-5.1}$	$9.7^{+7.7}_{-4.2}$	$0.79^{+3.00}_{-0.74}$
$\sigma_{\rm CARMENES\ VIS1}$	$4.31^{+1.00}_{-0.83}$	$1.2^{+1.1}_{-1.1}$	$1.2^{+1.1}_{-1.1}$	$0.45^{+1.40}_{-0.42}$	$0.6^{+1.4}_{-0.6}$	$0.26^{+1.10}_{-0.23}$	$0.27^{+1.20}_{-0.24}$	$0.61^{+1.40}_{-0.57}$
$\ln \mathcal{Z}$	–94.06	**–87.71**	–90.06	–90.39	–87.08	–87.86	–88.18	–87.05
$\Delta \ln \mathcal{Z}$	–6.35	**0.0**	–2.35	–2.68	0.64	–0.14	–0.46	0.66
CARMENES NIR1								
$P_{\rm stable}$	$2.269^{+0.016}_{-0.017}$	$2.286^{+0.016}_{-0.014}$	...	$2.264^{+0.049}_{-0.110}$	$2.287^{+0.023}_{-0.019}$	...	$2.270^{+0.051}_{-0.110}$	$2.288^{+0.025}_{-0.019}$
$K_{\rm stable}$	$18.0^{+2.6}_{-2.7}$	$21.8^{+3.9}_{-3.5}$	...	$16.3^{+4.1}_{-5.2}$	$20.7^{+4.3}_{-5.0}$	...	$16.6^{+4.0}_{-4.7}$	$20.9^{+4.2}_{-4.7}$
ecc.	0.0 (fixed)	$0.488^{+0.078}_{-0.130}$	...	0.0 (fixed)	$0.470^{+0.092}_{-0.200}$	...	0.0 (fixed)	$0.471^{+0.091}_{-0.190}$
$P_{\rm GP}$	...	...	$2.276^{+0.023}_{-0.042}$	$2.19^{+0.19}_{-0.11}$	$2.22^{+0.20}_{-0.15}$	$2.286^{+0.031}_{-0.031}$	$2.174^{+0.200}_{-0.097}$	$2.22^{+0.21}_{-0.15}$
$\sigma_{\rm GP,\ CARMENES\ NIR1}$	...	... $20.9^{+16.0}_{-7.4}$	16^{+21}_{-11}	$4.4^{+17.0}_{-4.3}$	$17.1^{+12.0}_{-6.8}$	$7.5^{+7.8}_{-6.2}$	$2.6^{+6.9}_{-2.5}$	
$\sigma_{\rm CARMENES\ NIR1}$	$0.97^{+5.30}_{-0.93}$	$0.34^{+2.80}_{-0.31}$	$0.28^{+2.30}_{-0.25}$	$0.30^{+2.70}_{-0.26}$	$0.25^{+2.10}_{-0.23}$	$0.43^{+4.10}_{-0.39}$	$0.31^{+2.90}_{-0.28}$	$0.26^{+2.20}_{-0.23}$
$\ln \mathcal{Z}$	**–109.92**	–108.95	–109.88	–108.72	–108.30	–111.07	–108.98	–108.32
$\Delta \ln \mathcal{Z}$	**0.0**	0.97	0.04	1.19	1.62	–1.15	0.94	1.60
HIRES + HARPS + CARMENES VIS + CARMENES NIR + HARPS-N + HPF								
$P_{\rm stable}$	$2.226228^{+0.000028}_{-0.000026}$	$2.227311^{+0.000018}_{-0.000019}$	...	$2.226329^{+0.000078}_{-0.000066}$	$2.226364^{+0.000900}_{-0.000088}$	...	$2.226345^{+0.000098}_{-0.000084}$	$2.22638^{+0.00095}_{-0.00010}$
$K_{\rm stable}$	$17.13^{+0.59}_{-0.58}$	$28.3^{+0.9}_{-1.0}$	...	$15.7^{+1.3}_{-4.5}$	$12.9^{+3.7}_{-2.7}$	...	$16.57^{+0.85}_{-2.20}$	$14.6^{+2.5}_{-4.0}$
$P_{\rm GP}$	...	...	$2.2245^{+0.0021}_{-0.0021}$	$2.2250^{+0.0022}_{-0.0021}$	$2.2252^{+0.0023}_{-0.0021}$	$2.22775^{+0.00054}_{-0.00067}$	$2.2270^{+0.0010}_{-0.0011}$	$2.22735^{+0.00095}_{-0.00120}$
ecc.	...	$0.183^{+0.022}_{-0.023}$	...	...	$0.072^{+0.100}_{-0.051}$	...	...	$0.072^{+0.099}_{-0.052}$
$\sigma_{\rm GP,\ HIRES}$	...	...	$25.6^{+4.6}_{-3.5}$	$20.8^{+3.6}_{-2.8}$	$21.1^{+3.7}_{-2.9}$	$23.9^{+5.0}_{-3.7}$	$19.6^{+3.5}_{-2.7}$	$19.9^{+3.8}_{-2.9}$
$\sigma_{\rm GP,\ HARPS}$	...	...	$33.2^{+6.9}_{-5.4}$	$25.5^{+5.6}_{-4.2}$	$26.0^{+5.8}_{-4.3}$	$25.9^{+5.9}_{-4.3}$	$20.6^{+4.7}_{-3.4}$	$21.2^{+4.7}_{-3.6}$
$\sigma_{\rm GP,\ CARMENES\ VIS1}$	...	...	$26.6^{+9.8}_{-6.6}$	$15.8^{+7.2}_{-4.8}$	$16.9^{+7.4}_{-5.1}$	$19.4^{+6.9}_{-4.8}$	$13.1^{+5.4}_{-3.6}$	$13.5^{+5.3}_{-3.8}$
$\sigma_{\rm GP,\ CARMENES\ NIR1}$	...	...	32^{+17}_{-13}	$0.78^{+13.00}_{-0.74}$	$4.2^{+25.0}_{-4.1}$	$18.5^{+23.0}_{-9.6}$	$0.26^{+2.40}_{-0.23}$	$1.4^{+9.4}_{-1.3}$
$\sigma_{\rm GP,\ HARPS\text{-}N1}$	...	...	$26.0^{+8.7}_{-5.6}$	$16.2^{+6.3}_{-4.1}$	$17.3^{+6.3}_{-4.5}$	$21.0^{+5.8}_{-4.3}$	$14.6^{+4.4}_{-3.3}$	$15.1^{+4.8}_{-3.4}$
$\sigma_{\rm GP,\ HARPS\text{-}N2}$	...	...	$15.8^{+7.7}_{-5.0}$	$10.3^{+7.3}_{-9.7}$	$7.5^{+8.3}_{-7.3}$	$30.2^{+10.0}_{-8.1}$	$21.6^{+7.9}_{-7.9}$	$20.7^{+8.5}_{-19.0}$
$\sigma_{\rm GP,\ CARMENES\ VIS2}$	...	...	$17.8^{+8.5}_{-5.1}$	$1.9^{+6.5}_{-1.9}$	$5.7^{+5.8}_{-5.4}$	$11.0^{+5.8}_{-3.3}$	$0.38^{+2.90}_{-0.35}$	$3.2^{+4.6}_{-3.0}$
$\sigma_{\rm GP,\ CARMENES\ NIR2}$	...	...	$15.7^{+14.0}_{-8.3}$	$7.1^{+11.0}_{-6.9}$	$2.3^{+12.0}_{-2.3}$	$9.3^{+12.0}_{-5.2}$	$6.8^{+9.7}_{-5.7}$	$2.4^{+9.2}_{-2.3}$
$\sigma_{\rm GP,\ HPF1}$	...	...	30^{+15}_{-12}	17^{+14}_{-16}	19^{+13}_{-18}	23^{+16}_{-14}	$4.8^{+16.0}_{-4.7}$	13^{+12}_{-12}
$\sigma_{\rm GP,\ HPF2}$	...	...	$8.4^{+2.6}_{-2.0}$	$9.2^{+2.7}_{-2.5}$	$8.2^{+3.0}_{-2.7}$	$6.1^{+2.7}_{-1.8}$	$7.8^{+2.6}_{-1.8}$	$7.2^{+2.5}_{-1.9}$
$\sigma_{\rm HIRES}$	$17.0^{+2.0}_{-1.7}$	$19.5^{+2.5}_{-2.1}$	$1.4^{+1.2}_{-1.3}$	$1.3^{+1.2}_{-1.2}$	$1.3^{+1.1}_{-1.2}$	$0.78^{+1.20}_{-0.73}$	$0.69^{+1.20}_{-0.64}$	$0.59^{+1.30}_{-0.55}$
$\sigma_{\rm HARPS}$	$18.0^{+2.1}_{-1.7}$	$12.2^{+1.5}_{-1.2}$	$1.05^{+0.44}_{-0.46}$	$0.93^{+0.48}_{-0.67}$	$0.92^{+0.47}_{-0.66}$	$0.12^{+0.48}_{-0.10}$	$0.108^{+0.410}_{-0.086}$	$0.094^{+0.370}_{-0.073}$
$\sigma_{\rm CARMENES\ VIS1}$	$7.4^{+1.4}_{-1.1}$	$2.33^{+0.84}_{-0.82}$	$0.48^{+1.40}_{-0.44}$	$0.59^{+1.50}_{-0.55}$	$0.61^{+1.40}_{-0.57}$	$0.24^{+1.10}_{-0.21}$	$0.26^{+1.10}_{-0.23}$	$0.35^{+1.10}_{-0.31}$
$\sigma_{\rm CARMENES\ NIR1}$	$1.2^{+5.3}_{-1.2}$	$11.6^{+3.2}_{-2.7}$	$0.60^{+4.60}_{-0.56}$	$1.4^{+5.8}_{-1.4}$	$1.4^{+6.1}_{-1.4}$	$0.89^{+6.00}_{-0.85}$	$1.8^{+5.5}_{-1.7}$	$2.0^{+5.9}_{-1.9}$
$\sigma_{\rm HARPS\text{-}N1}$	$11.1^{+1.4}_{-1.2}$	$4.05^{+0.81}_{-0.62}$	$1.58^{+0.37}_{-0.32}$	$1.62^{+0.37}_{-0.33}$	$1.62^{+0.37}_{-0.32}$	$0.40^{+0.62}_{-0.36}$	$0.46^{+0.62}_{-0.42}$	$0.51^{+0.58}_{-0.45}$
$\sigma_{\rm HARPS\text{-}N2}$	$9.1^{+1.7}_{-1.3}$	$16.6^{+3.1}_{-2.4}$	$4.2^{+1.4}_{-1.1}$	$4.9^{+1.9}_{-1.5}$	$5.1^{+1.6}_{-1.6}$	$0.18^{+1.20}_{-0.15}$	$0.25^{+2.90}_{-0.22}$	$0.42^{+5.00}_{-0.38}$
$\sigma_{\rm CARMENES\ VIS2}$	$0.098^{+0.410}_{-0.077}$	$8.9^{+1.9}_{-1.5}$	$0.095^{+0.380}_{-0.075}$	$0.098^{+0.380}_{-0.077}$	$0.10^{+0.40}_{-0.08}$	$0.097^{+0.380}_{-0.076}$	$0.092^{+0.370}_{-0.071}$	$0.110^{+0.360}_{-0.086}$
$\sigma_{\rm CARMENES\ NIR2}$	$5.6^{+4.5}_{-5.3}$	$6.1^{+4.0}_{-5.8}$	$0.3^{+2.8}_{-0.3}$	$0.28^{+2.50}_{-0.25}$	$0.27^{+2.30}_{-0.24}$	$0.3^{+3.0}_{-0.3}$	$0.29^{+2.60}_{-0.26}$	$0.36^{+2.80}_{-0.32}$
$\sigma_{\rm HPF1}$	$10.2^{+5.1}_{-2.9}$	$7.6^{+4.1}_{-2.2}$	$0.89^{+12.00}_{-0.84}$	$2.2^{+10.0}_{-2.1}$	$1.4^{+10.0}_{-1.3}$	$1.7^{+14.0}_{-1.6}$	$7.9^{+6.0}_{-7.5}$	$3.9^{+8.4}_{-3.7}$
$\sigma_{\rm HPF2}$	$12.1^{+1.9}_{-1.5}$	$20.7^{+3.0}_{-2.5}$	$2.98^{+0.82}_{-0.65}$	$2.50^{+0.71}_{-0.62}$	$2.61^{+0.75}_{-0.62}$	$2.90^{+0.72}_{-0.63}$	$2.39^{+0.72}_{-0.74}$	$2.47^{+0.73}_{-0.69}$
$\ln \mathcal{Z}$	–1143.31	–1143.38	–1002.17	–992.50	–993.37	–966.77	**-963.40**	–965.73
$\Delta \ln \mathcal{Z}$	–179.91	–179.99	–38.77	–29.10	–29.98	–3.37	**0.0**	–2.33

Notes. The selected best model is boldfaced (refer to Sect. 6 for details on the priors used, model choice, and discussion of results). The columns refer to which model was being used, whereas the rows correspond to the model parameter. A larger, positive $\Delta \ln \mathcal{Z}$ value indicates a better model. Priors for the NIR arm are slightly different because of the lower data quality, hence, the period priors are wider, U(2.2 days, 2.5 days).

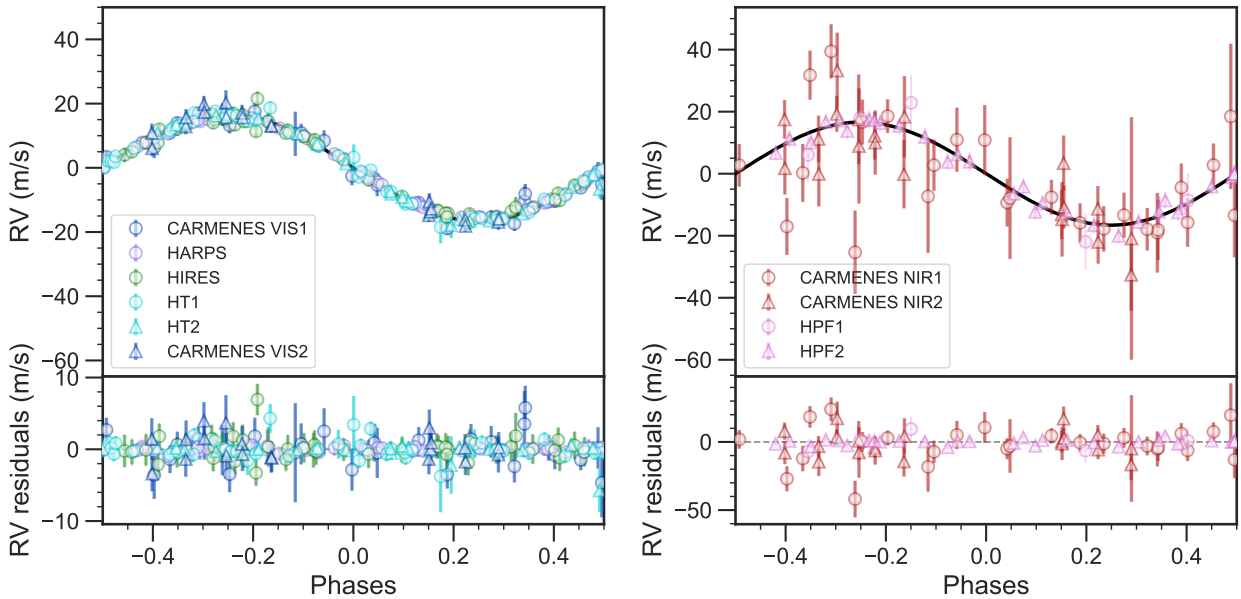

Fig. 7. Phase-folded plots for the optical (*left*) and near-infrared (*right*) instruments using the circular Keplerian + dSHO-GP model after subtracting the GP component out. The first subset of any given instrument is represented with a circle, whereas the second subset by a triangle, when applicable. The y-axis ranges are consistent between the two plots, except for the residual plots to better visualize the scatter around the fit.

and the phase-folded plots for the best model, namely the mixed model, are shown in Fig. 7.

To summarize our findings, we have the following takeaway points:

– The CARMENES-VIS1 data alone prefer an eccentric Keplerian ($e \sim 0.19$) model. This is in agreement with the HARPS-N data from C20. Whereas, the CARMENES-NIR1 data alone prefer a circular Keplerian, that is, a sinusoid.

– The amplitude between the two CARMENES seasons decreased in both instruments. Namely, from $28.43^{+0.94}_{-0.98}$ m s^{-1} to $17.02^{+0.63}_{-0.62}$ m s^{-1} in the VIS channel, and from $18.0^{+2.6}_{-2.7}$ m s^{-1} to $9.2^{+3.0}_{-2.6}$ m s^{-1} in the NIR channel.

– Combining both seasons of the CARMENES data (i.e., VIS1+VIS2 and NIR1+NIR2), a circular Keplerian is preferred.

– Combining all data sets, the mixed circular Keplerian + GP model provides the best fit, for either GP used (QP-GP or dSHO-GP). This signifies that there is a stable and variable component in the data.

– The $K_{\rm stable}$ of the preferred model (mixed circular Keplerian + dSHO-GP model) is 16.6 ± 2.2 m s^{-1}. The amplitude of the GP component ($\sigma_{\rm GP,\,inst}$) is consistent with 0 for the near-IR instruments, except for HPF2 ($\sigma_{\rm GP,\,HPF2} = 7.8 \pm 2.6$ m s^{-1}). For the optical instruments, the earlier data, namely with HARPS, HIRES, have similar sigmas ($\sigma_{\rm GP,\,inst} \sim 20$ m s^{-1}) as well as the overlapping data, with VIS1 and HT1 ($\sigma_{\rm GP,\,inst} \sim 13$ m s^{-1}). For VIS2, it was consistent with zero and for HT2, it was higher with $\sigma_{\rm GP,\,inst} \sim 22$ m s^{-1}.

– The difference in evidence between a mixed model and a GP-only model depended on the GP kernel choice (i.e., $\Delta \ln \mathcal{Z} \sim 3.5$ and $\Delta \ln \mathcal{Z} \sim 10$ when considering a dSHO-GP and QP-GP kernel, respectively).

7. Discussion and future outlook

In this analysis, we presented new CARMENES optical and near-IR data that cover a wide wavelength range well into the red part of the spectrum to test the origin of the 2.23 days signal found in the RVs for AD Leo. The presence of stellar activity is supported with CARMENES through the proof of wavelength- and time-dependence. With the CARMENES data alone, the shape of the wavelength dependence of the RV amplitude can be attributed to a star-spot configuration following Reiners et al. (2010). Between the two CARMENES seasons, the amplitude decreased in both instruments. Specifically, from $28.43^{+0.94}_{-0.98}$ m s^{-1} to $17.02^{+0.63}_{-0.62}$ m s^{-1} in the VIS channel, and from $18.0^{+2.6}_{-2.7}$ m s^{-1} to $9.2^{+3.0}_{-2.6}$ m s^{-1} in the near-IR channel when modeling the signals as pure sinsuoidal variations. C20 also found an amplitude decrease between the HARPS-N and GIANO-B data, that is, from 33 m s^{-1} to less than 23 m s^{-1} between the instruments and from 33 m s^{-1} to 13 m s^{-1} between seasons. However, given the large errorbars of the GIANO-B data (~20 m s^{-1}), it was only possible to identify an amplitude decrease, but not to constrain whether there even is a signal present in these data at 2.23 days. Likewise, the high-precision near-IR data from HPF show a much smaller RV amplitude (R20), inconsistent with the higher RV amplitude in the optical, and there is also a discrepancy even between HPF seasons, namely, the RMS scatter dropped from 23 m s^{-1} to 6.4 m s^{-1}. This decrease in amplitude is also seen in the overlapping, optical HARPS-N data and second season of CARMENES data (see again Fig. 2). Nonetheless, both our results and those in C20 and R20 agree that the signal's amplitude does indeed decrease rather than increase, indicating that AD Leo is entering a lower-activity phase. We conclude that the effect of the spots on the RVs is dominated by temperature differences rather than the Zeeman effect (see Reiners et al. 2013), in accordance with the other evidence at hand such as photometric variability (presented in T18).

7.1. Possibility of stable stellar-spot signal

It is common practice to model activity-induced RVs with GPs (e.g., Rajpaul et al. 2015, and further citations), as they are nondeterministic models that can sufficiently fit stochastic modulations. Provided that the evidence against a planet outweighs that in favor of a planet, our understanding was to expect that the GP-only model should have been adequate enough in accounting for the stellar activity, with the assumption that the signal

in AD Leo is purely stellar activity induced. The modeling instead showed that neither a stable-only (i.e., sinusoid) model nor red-noise-only (i.e., GP-only) model can correctly describe the whole data set (Table 3). A mix of a stable and variable component is rather the preferred model, where the stable model has an amplitude of $K_{\rm stable} = 16.6 \pm 2.2\,{\rm m\,s^{-1}}$, lower than the value of $19\,{\rm m\,s^{-1}}$ proposed by T18. We do not claim that the stable component is solely due to a planetary companion as it could perhaps be also due to the persistent presence of a circumpolar stellar spot imposing a constant behavior, or even a mixture of both. Thus, we set an 3σ upper limit (i.e., from $K_{\rm stable} = 16.6 \pm 3 \times 2.2\,{\rm m\,s^{-1}}$) of 27 $M_\oplus$ (or 0.084 $M_{\rm Jup}$) for a putative planetary companion, in comparison to the proposed mass of ~0.2 $M_{\rm Jup}$ by T18. Focusing on the amplitudes of the GP kernel of the mixed model, we found that those of the earlier optical RV data, specifically HARPS and HIRES ($\sigma_{\rm GP,\,inst} \sim 20\,{\rm m\,s^{-1}}$), were higher than most of the more recent optical data ($\sigma_{\rm GP,\,inst} \lesssim 13\,{\rm m\,s^{-1}}$). These values support the assumption that the star was more active earlier and is entering a less active phase (Sect. 2.2). The only exception was with HT2, with $\sigma_{\rm GP,\,HT2} \sim 22\,{\rm m\,s^{-1}}$, an even higher value. The GP amplitudes of near-IR spectrographs were consistent with $\sigma_{\rm GP,\,inst} \sim 0\,{\rm m\,s^{-1}}$, except for HPF2 ($\sigma_{\rm GP,\,HPF2} \sim 8\,{\rm m\,s^{-1}}$). The data from the two instruments that stand out (i.e., HT2 and HPF2) were contemporaneously taken, indicating that there was some phase shift between the stable and variable component during this time period. A better understanding of how model comparison can behave given a purely stellar-activity induced signal would be necessary to determine if such a result is even expected (see also Sect. 7.2 for future suggestions). Additionally, our analysis of recomputing the RVs, considering only those spectral lines unaffected by stellar activity, still showed some strong significant periodicity at 2.23 days (Fig. 6), unlike for other known active stars where the signals had disappeared (Lafarga, priv. comm.).

Nonetheless, this should raise the question of whether a signal with an amplitude of $\sim 17\,{\rm m\,s^{-1}}$ that is fully stable over all these observations (~19 yr) in such an M dwarf is possible. In fact, it is not so surprising that spot-induced RV fluctuations for M dwarfs are long-lived (e.g., Günther et al. 2022; Quirrenbach et al. 2022). Though evidence of stable stellar activity behavior had previously been shown in photometry (e.g., GJ 1243, Davenport et al. 2020) and RVs (e.g., α Tau, Hatzes et al. 2015) over time, our paper demonstrates the first case for modeling RVs over time and wavelength. Future studies performing simulations with software packages such as `StarSim 2.0` (Herrero et al. 2016) or `SOAP 2.0` (Dumusque et al. 2014) using various star-spot configurations may also shed light on why a signal can stay persistent over many years (Herrero et al. 2016; Rosich et al. 2020). Utilizing `StarSim 2.0` to compare RV-CRX correlations between simulated and real data as performed by Baroch et al. (2020), with YZ CMi as a case study, could be beneficial in determining the star-spot temperature difference, the star-spot filling factor, and the location of the spot. A first test with a simple assumption (i.e., one big polar spot) could reproduce well the RVs and CRX values of AD Leo for the CARMENES VIS data (Baroch priv. comm.). But such an approach can become degenerate when considering so many instruments and various star-spot configurations, and a planetary signal would act as an achromatic offset to the RVs and CRX.

7.2. Current limitations

AD Leo is a prime case study for M dwarfs to explore the possibility of a planetary signal with an orbital period indistinguishably close to its stellar host's rotation period. Given its rich multi-wavelength spectroscopic monitoring over a large time baseline, there are no other targets with such an extensive data set coverage. Even then, we showed that there are apparent holes in our current state of research in this field in which studies to address them would require proposals, dedicated surveys and telescope time. In essence, we are either limited by our modeling approaches, by our astrophysical knowledge of star-spot configurations, or a combination of both. In order to progress and disentangle this problem, we propose the following, in no particular order.

7.2.1. Simultaneous multiband photometry

The shape of the curve in Fig. 5 is determined by stellar activity behavior, whereas the presence of a planet would simply act as an offset across the wavelength space. Even when doubling (or halving) the number of available spectroscopic data points, disentangling the contribution of a planetary signal within this curve still persists as a degenerate problem. Obtaining continuous and simultaneous multiband photometry would help in painting a better picture of the stellar-spot map distribution. In doing so, this can then be translated by forward modeling to determine the stellar-activity induced RVs (e.g., via `Starsim 2.0` or `SOAP 2.0`; Herrero et al. 2016; Dumusque et al. 2014). The residual between these computed RVs and those obtained would indicate the contribution of the Keplerian component. However, the caveat is, that spot configurations on the stellar surface can vary with time. Thus, continuous photometry would only apply to simultaneously taken RVs.

7.2.2. A better-suited RV data set for spectral line analyses

In the absence of available photometric facilities, the approach of selecting spectral lines not affected by activity seems promising. This line-by-line approach has been successfully applied to other stars (e.g., Dumusque 2018; Wise et al. 2018; Cretignier et al. 2020). In the case for AD Leo, it is difficult to decipher whether it was the target itself or the relatively new method that resulted in an inconclusive outcome. Perhaps the RVs were not as affected by the stellar spots (i.e., due to the pole-on inclination), the RV amplitude was not as large as the others, or there were not enough data points to strengthen the correlation plots by establishing a statistically stronger correlation. Definitely, if overall activity decreases, then it would be more difficult to pick up the activity within certain spectral lines. Hence, observing a star when it is in its most active phase would constitute the ideal data set. Additionally, our spectral line analysis should be applied to a wider wavelength range (e.g., HARPS) as well to determine if the signal disappears. Another possible explanation could be that all lines are inherently affected by activity to some degree. Nonetheless, determining the ideal targets for this technique as well as developing the method further will be paramount in suppressing activity for future M-dwarf studies.

7.2.3. Magnetic star-planet interaction

The radio bursts thus far observed for the AD Leo system (outlined in Sect. 2.5) suggest an excess that is unaccounted for. A possible scenario to justify the discrepancy could be due to sub-Alfvénic interaction of the stellar magnetosphere with an orbiting body, in this case with a putative planet around AD Leo, which has $P_{\rm orb} = P_{\rm rot}$. This magnetic interaction between the star and a planet (Magnetic Star-Planet Interaction; MSPI) would be responsible for producing: (1) an enhancement of the magnetic

activity of the star, and (2) the long-duration radio emission as that detailed in Sect. 2.5, both effects of which are modulated in phase with the orbital period of the planet. In a star like AD Leo, the difficulties for detecting this modulation are that this target is seen nearly pole-on ($i \sim 13$ deg) and that a putative planet orbit is synchronized with the stellar rotation. This produces a weaker MSPI, as it depends on the relative velocity of the planet with respect to the magnetosphere of the star (Lanza 2009, 2012) and makes it difficult to disentangle it from stellar intrinsic activity. However, the presence of such a planet could explain the need for the stable component and part of its semi-amplitude ($K_{\rm stable} < 16.6\,{\rm m\,s^{-1}}$) seen in the RVs in this work. MSPI would show as a hot spot in the chromosphere that would mainly affect the chromospheric activity indicators such as $\log R'_{\rm HK}$ from the Ca II H&K lines, not available in the CARMENES data set but covered by HARPS.

Within this scenario, we followed the prescriptions in Appendix B of Pérez-Torres et al. (2021) to estimate the flux density expected to arise from the interaction between a putative planet and its host star. We assume for simplicity an isothermal Parker wind with a temperature of $(2-3)\times10^6$ K, and a density of $10^{7-8}\,{\rm cm^{-3}}$ at the base of the corona. Since the hypothetical planet would be very close to its host star, we find that the planet is in the sub-Alfvénic regime, which makes it possible that energy and momentum can be carried upstream of the flow along Alfvén wings. We estimate that the radio flux in the few GHz band, arising from star-planet interaction, is in the range from less than about 0.1 mJy and up to a few mJy, or even higher, depending on the stellar wind parameters at both the corona and at the orbital position of the planet. We therefore encourage a campaign for simultaneous monitoring of AD Leo in both optical (i.e., spectroscopy, including Ca II H&K lines, and photometry) and in radio wavelengths to test the star-planet (sub-Alfvénic) interaction scenario. The detection of a correlation in the radio signal with the orbital period would be the smoking gun of sub-Alfvénic interaction, serving as an argument in support of the presence of a planet in the system.

7.2.4. Application of GP models for red-noise correlated signals

Additional data may not be what is necessary as much as is a better understanding of the astrophysical effects stellar spots impose on the star and how we choose to model them through nonphysically motivated means. The usage of GPs is currently the most popular approach in the RV field for modeling stellar activity. That being said, the most commonly used kernels (i.e., QP-GP, dSHO-GP) are not completely physically motivated, but nonetheless serve as a very good approximation to our aim of describing the quasi-periodic behavior. They can play a vital role, especially when trying to search for low-mass planets with low amplitudes among noisy data (e.g., Stock et al. 2020; Demangeon et al. 2021; Faria et al. 2022).

The problem is, however, that we do not know just how effective the GPs are in serving their purpose and what limitations and consequences on (planetary) parameters they particularly have. Perhaps, the choice of the GP for different time baselines could be also of importance, as is the case for AD Leo (see Sect. 6), considering there are, for the time being, too many unknowns that can lead to misinterpretations. Newer implementations of GP kernels with a potentially better physical interpretation of stellar processes could become essential (e.g., Perger et al. 2021; Luger et al. 2021). Applying these models to real data sets turns out to not be the solution, as it becomes complicated to correctly interpret the results. For this reason, these models should be compared against each other on controlled, simulated RV time series. A more in-depth study could include simulating RV time series by injecting solely stellar-activity-induced signals and a mixture of stellar activity and planetary components for a general grasp (Stock et al. 2022). One step further would be to specifically simulate the stellar characteristics of AD Leo, together with the time stamps and various wavelengths. Even here, the limitation of our knowledge of spot distribution maps and correctly choosing the correct one persists.

In future potential cases where there is a presumed planetary and stellar activity signal with two instruments covering a wide wavelength range, for instance, with CARMENES, it is crucial to adequately model the wavelength dependence of the stellar activity to ensure the most precise planetary parameters. More so for M-dwarf stars considering that their stellar rotation periods would often correlate to the orbital periods of planets residing in the habitable zone (Newton et al. 2016). AD Leo in this regard is an interesting case study to perform such fits when considering real data, however, simulated data sets may offer a more controlled environment to test the effectiveness of our current modeling techniques. Either way, AD Leo certainly serves as a particularly intriguing system for studying the impact of a stable spot periodicity on the search for planetary signals.

7.2.5. Using auxiliary data to correct for stellar activity

Another promising procedure is to include the stellar activity indicators as auxiliary data to try to detrend the RVs, commonly done so as linear components (e.g., Anglada-Escudé et al. 2016) or within the GP kernel (e.g., Suárez Mascareño et al. 2020; Cale et al. 2021; Barragán et al. 2022) in regards to planet detection. Likewise, this technique is being carried out in a sole stellar activity context (Jeffers et al. 2022; Cardona Guillén et al. 2022), with particular attention to not only detrending with various indicators, but also to characterizing the behavior of the correlations. Specifically, this "closed-loop" relation is becoming more prevalent, as already exhibited with known active M-dwarf stars such as YZ CMi (Zechmeister et al. 2018; Baroch et al. 2020), EV Lac (Jeffers et al. 2022), and GJ 674 (Bonfils et al. 2007), and now for AD Leo as displayed in the RV-CRX and RV-BIS correlations (Fig. C.1). Subtracting out the CRX dependency can improve the rms of the RVs, though it is nearly impossible to obtain a straight line from the correction, that is, completely removing all of the stellar activity, even in cases with very high signal-to-noise ratios and very dense sampling (e.g., factor of three improvement for EV Lac; Jeffers et al. 2022). For our case of AD Leo (Sect. 4.1), the CRX detrending improved the rms roughly by a factor of two for VIS1 (from $18.5\,{\rm m\,s^{-1}}$ to $9.2\,{\rm m\,s^{-1}}$).

In this line, a relatively recent technique is that of using spectropolarimetric measurements to correct the RVs of the variability introduced by the activity. The data are used to derived precise RVs and to obtain maps of the magnetic field and the distribution of surface inhomogeneities. These maps are then used to obtain a model RV curve, which are the subtracted from the observed RVs. The removal of activity variations with this technique decreased the amplitude of the RV curve in V830 Tau by a factor 10, which allowed the detection of a hot Jupiter orbiting this very young T Tauri star (Donati et al. 2016).

While these approaches are encouraging, they still poses limitations when considering a putative planetary signal whose orbital period is equal to the rotational period because the same issue, as mentioned already above, of degeneracy still holds true. Again, a systematic simulated analysis of forward modeling RVs

and stellar activity indicators could be key in understanding what correlations to expect and how to properly detrend them.

8. Conclusions

In this paper we presented new CARMENES optical and near-infrared spectroscopic data for a known nearby, active M dwarf, AD Leo. The stellar rotation period of 2.23 days is clearly present in the RVs, and we address the question of whether there could be a planet orbiting with the same periodicity, $P_{\rm orb} = P_{\rm rot}$. Taking advantage of the wide wavelength range of the CARMENES instrument, we demonstrated the shape of the wavelength dependency of the RV semi-amplitudes to be in agreement with what is expected for a star-spot temperature difference configuration. The strong anticorrelation found between CRX-RV and BIS-RV for the CARMENES VIS data were additional signs of stellar activity. In addition, we recomputed RVs using spectral lines unaffected by stellar activity, which has not been done before for AD Leo, and found that there was still some significant residual power at the rotational period.

When incorporating all available RVs (HARPS, HIRES, CARMENES, and the more recent HARPS-N, GIANO-B, and HPF data), it became evident that the signal has undergone various amplitude fluctuations as well as phase shifts, and this is behavior that cannot be attributed to the presence of a planetary companion. However, a closer look into the model comparison showed that a mixed model of a stable plus a quasi-periodic red-noise model best explained the data, where the stable component had a semi-amplitude of $K_{\rm stable} = 16.6 \pm 2.2\,{\rm m\,s^{-1}}$, setting a 3σ upper limit on the mass of a putative planet, $27\,M_\oplus$ ($= 0.084\,M_{\rm Jup}$). Based on all this evidence, our current machinery, and the given data at hand, we conclude we cannot unequivocally prove, or even disprove, the 2.23 days periodic signal found in AD Leo to be solely due to stellar activity. We therefore suggest to obtain simultaneous photometry and spectroscopy in various wavelengths accompanied by radio observations, and complemented with a clearer insight of stellar activity behavior on measurements via simulated time series to break the degeneracy.

Acknowledgements. CARMENES is an instrument for the Centro Astronómico Hispano-Alemán de Calar Alto (CAHA, Almería, Spain). CARMENES was funded by the Max-Planck-Gesellschaft (MPG), the Consejo Superior de Investigaciones Científicas (CSIC), the Ministerio de Economía y Competitividad (MINECO) and the European Regional Development Fund (ERDF) through projects FICTS-2011-02, ICTS-2017-07-CAHA-4, and CAHA16-CE-3978, and the members of the CARMENES Consortium (Max-Planck-Institut für Astronomie, Instituto de Astrofísica de Andalucía, Landessternwarte Königstuhl, Institut de Ciències de l'Espai, Institut für Astrophysik Göttingen, Universidad Complutense de Madrid, Thüringer Landessternwarte Tautenburg, Instituto de Astrofísica de Canarias, Hamburger Sternwarte, Centro de Astrobiología and Centro Astronómico Hispano-Alemán), with additional contributions by the MINECO, the Deutsche Forschungsgemeinschaft (DFG) through the Major Research Instrumentation Programme and Research Unit FOR2544 "Blue Planets around Red Stars", the Klaus Tschira Stiftung, the states of Baden-Württemberg and Niedersachsen, and by the Junta de Andalucía. We acknowledge financial support from the Agencia Estatal de Investigación of the Ministerio de Ciencia, Innovación y Universidades and the ERDF through projects PID2019-109522GB-C51/2/3/4 PGC2018-098153-B-C33 AYA2017-84089, AYA2016-79425-C3-1/2/3-P, ESP2016-80435-C2-1-R, and the Centre of Excellence "Severo Ochoa" and "María de Maeztu" awards to the Instituto de Astrofísica de Canarias (SEV-2015-0548), Instituto de Astrofísica de Andalucía (SEV-2017-0709), and Centro de Astrobiología (MDM-2017-0737), the Generalitat de Catalunya/CERCA programme, and the DFG under Research Unit FOR2544. T.T. acknowledges support by the DFG Research Unit FOR 2544 "Blue Planets around Red Stars" project no. KU 3625/2-1. T.T. further acknowledges support by the BNSF program "VIHREN-2021" project No. КП-06-ДВ/5. This research has made use of the ESO Science Archive Facility and the CARMENES data archive at CAB (CSIC-INTA). Based on observations collected at the European Southern Observatory under ESO programs 072.C-0488, 191.C-0505, and 192.C-0224.

References

Abell, G. O. 1959, PASP, 71, 517
Alonso-Floriano, F. J., Morales, J. C., Caballero, J. A., et al. 2015, A&A, 577, A128
Amado, P. J., Bauer, F. F., Rodríguez López, C., et al. 2021, A&A, 650, A188
Ambikasaran, S., Foreman-Mackey, D., Greengard, L., Hogg, D. W., & O'Neil, M. 2015, IEEE Trans. Pattern Anal. Mach. Intell., 38, 252
Anderson, E. R., Duvall, Thomas L., J., & Jefferies, S. M. 1990, ApJ, 364, 699
Anglada-Escudé, G., Amado, P. J., Barnes, J., et al. 2016, Nature, 536, 437
Argelander, F. W. A. 1861, Bonner Sternverzeichniss, 2. (Adolph Marcus)
Astudillo-Defru, N., Delfosse, X., Bonfils, X., et al. 2017, A&A, 600, A13
Balega, Y. Y., & Balega, I. I. 1985, Sov. Astron. Lett., 11, 47
Balega, I., Bonneau, D., & Foy, R. 1984, A&AS, 57, 31
Baluev, R. V. 2009, MNRAS, 393, 969
Barnes, J. R., Jenkins, J. S., Jones, H. R. A., et al. 2014, MNRAS, 439, 3094
Baroch, D., Morales, J. C., Ribas, I., et al. 2020, A&A, 641, A69
Barrado y Navascués, D. 1998, A&A, 339, 831
Barragán, O., Aigrain, S., Rajpaul, V. M., & Zicher, N. 2022, MNRAS, 509, 866
Bauer, F. F., Reiners, A., Beeck, B., & Jeffers, S. V. 2018, A&A, 610, A52
Bauer, F. F., Zechmeister, M., Kaminski, A., et al. 2020, A&A, 640, A50
Bayliss, D., Gillen, E., Eigmüller, P., et al. 2018, MNRAS, 475, 4467
Bidelman, W. P. 1985, ApJS, 59, 197
Boeshaar, P. C. 1976, Ph.D. Thesis. Ohio State University, Columbus
Bonfils, X., Mayor, M., Delfosse, X., et al. 2007, A&A, 474, 293
Bonfils, X., Delfosse, X., Udry, S., et al. 2013, A&A, 549, A109
Borucki, W. J., Koch, D., Basri, G., et al. 2010, Science, 327, 977
Brandt, T. D., Kuzuhara, M., McElwain, M. W., et al. 2014, ApJ, 786, 1
Buccino, A. P., Lemarchand, G. A., & Mauas, P. J. D. 2007, Icarus, 192, 582
Butler, R. P., Vogt, S. S., Laughlin, G., et al. 2017, AJ, 153, 208
Caballero, J. A., Cortés-Contreras, M., Alonso-Floriano, F. J., et al. 2016, in 19th Cambridge Workshop on Cool Stars, Stellar Systems, and the Sun (CS19), 148
Caballero, J. A., Gonzalez-Alvarez, E., Brady, M., et al. 2022, A&A, 665, A120
Cale, B. L., Reefe, M., Plavchan, P., et al. 2021, AJ, 162, 295
Cardona Guillén, C., Béjar, V. J. S., Lodieu, N., et al. 2022, A&A, submitted
Carleo, I., Malavolta, L., Lanza, A. F., et al. 2020, A&A, 638, A5
Chadney, J. M., Galand, M., Koskinen, T. T., et al. 2016, A&A, 587, A87
Cifuentes, C., Caballero, J. A., Cortés-Contreras, M., et al. 2020, A&A, 642, A115
Claudi, R., Benatti, S., Carleo, I., et al. 2017, Eur. Phys. J. Plus, 132, 364
Cortés-Contreras, M. 2016, Ph.D. Thesis, Universidad Complutense de Madrid, Spain
Cortés-Contreras, M., Béjar, V. J. S., Caballero, J. A., et al. 2017, A&A, 597, A47
Cosentino, R., Lovis, C., Pepe, F., et al. 2012, in Ground-based and Airborne Instrumentation for Astronomy IV, eds. I. S. McLean, S. K. Ramsay, & H. Takami, 8446, International Society for Optics and Photonics (SPIE), 657
Crespo-Chacón, I., Montes, D., García-Alvarez, D., et al. 2006, A&A, 452, 987
Cretignier, M., Dumusque, X., Allart, R., Pepe, F., & Lovis, C. 2020, A&A, 633, A76
Daemgen, S., Siegler, N., Reid, I. N., & Close, L. M. 2007, ApJ, 654, 558
Davenport, J. R. A., Mendoza, G. T., & Hawley, S. L. 2020, AJ, 160, 36
Dawson, R. I., & Fabrycky, D. C. 2010, ApJ, 722, 937
Demangeon, O. D. S., Zapatero Osorio, M. R., Alibert, Y., et al. 2021, A&A, 653, A41
Desort, M., Lagrange, A. M., Galland, F., Udry, S., & Mayor, M. 2007, A&A, 473, 983
Docobo, J. A., Tamazian, V. S., Balega, Y. Y., & Melikian, N. D. 2006, AJ, 132, 994
Donati, J. F., Moutou, C., Malo, L., et al. 2016, Nature, 534, 662
Donati, J. F., Kouach, D., Moutou, C., et al. 2020, MNRAS, 498, 5684
Dumusque, X. 2018, A&A, 620, A47
Dumusque, X., Boisse, I., & Santos, N. C. 2014, ApJ, 796, 132
Engelkemeir, D. 1959, PASP, 71, 522
Engle, S. G., Guinan, E. F., & Mizusawa, T. 2009, in American Institute of Physics Conference Series, 1135, Future Directions in Ultraviolet Spectroscopy: A Conference Inspired by the Accomplishments of the Far Ultraviolet Spectroscopic Explorer Mission, eds. M. E. van Steenberg, G. Sonneborn, H. W. Moos, & W. P. Blair, 221
Espinoza, N., Kossakowski, D., & Brahm, R. 2019, MNRAS, 490, 2262
Faria, J. P., Suárez Mascareño, A., Figueira, P., et al. 2022, A&A, 658, A115
Favata, F., Micela, G., & Reale, F. 2000, A&A, 354, 1021

Foreman-Mackey, D., Agol, E., Ambikasaran, S., & Angus, R. 2017, AJ, 154, 220
Fuhrmeister, B., Czesla, S., Nagel, E., et al. 2022, A&A, 657, A125
Fulton, B. J., Petigura, E. A., Blunt, S., & Sinukoff, E. 2018, PASP, 130, 044504
Gaia Collaboration (Smart, R. L., et al.) 2021, A&A, 649, A6
Gaidos, E., Mann, A. W., Lépine, S., et al. 2014, MNRAS, 443, 2561
Gliese, W. 1957, Astron. Rechen-Institut Heidelberg Mitteilungen Ser. A, 8, 1
Gomes da Silva, J., Santos, N. C., Bonfils, X., et al. 2011, A&A, 534, A30
Gordon, K. C., & Kron, G. E. 1949, PASP, 61, 210
Grandjean, A., Lagrange, A. M., Keppler, M., et al. 2020, A&A, 633, A44
Günther, M. N., Berardo, D. A., Ducrot, E., et al. 2022, AN, 163, 144
Gurzadyan, G. A. 1971, A&A, 13, 348
Hatzes, A. P. 2016, A&A, 585, A144
Hatzes, A. P., Cochran, W. D., Endl, M., et al. 2015, A&A, 580, A31
Hawley, S. L., & Pettersen, B. R. 1991, ApJ, 378, 725
Hawley, S. L., Allred, J. C., Johns-Krull, C. M., et al. 2003, ApJ, 597, 535
Haywood, R. D., Collier Cameron, A., Queloz, D., et al. 2014, MNRAS, 443, 2517
Herrero, E., Ribas, I., Jordi, C., et al. 2016, A&A, 586, A131
Hojjatpanah, S., Figueira, P., Santos, N. C., et al. 2019, A&A, 629, A80
Hunt-Walker, N. M., Hilton, E. J., Kowalski, A. F., Hawley, S. L., & Matthews, J. M. 2012, PASP, 124, 545
Jeffers, S. V., Schöfer, P., Lamert, A., et al. 2018, A&A, 614, A76
Jeffers, S. V., Barnes, J. R., Schöfer, P., et al. 2022, A&A, 663, A27
Johnson, H. L., & Morgan, W. W. 1953, ApJ, 117, 313
Jones, D. E., Stenning, D. C., Ford, E. B., et al. 2017, ArXiv e-prints, [arXiv:1711.01318]
Keenan, P. C., & McNeil, R. C. 1989, ApJS, 71, 245
Kirkpatrick, J. D., Henry, T. J., & McCarthy, Donald W., J. 1991, ApJS, 77, 417
Klutsch, A., Freire Ferrero, R., Guillout, P., et al. 2014, A&A, 567, A52
Kotani, T., Tamura, M., Suto, H., et al. 2014, SPIE Conf. Ser., 9147, 914714
Kotani, T., Tamura, M., Nishikawa, J., et al. 2018, SPIE Conf. Ser., 10702, 1070211
Kürster, M., Endl, M., Rouesnel, F., et al. 2003, in ESA Special Publication, 539, Earths: DARWIN/TPF and the Search for Extrasolar Terrestrial Planets, eds. M. Fridlund, T. Henning, & H. Lacoste, 485
Lafarga, M., Ribas, I., Lovis, C., et al. 2020, A&A, 636, A36
Lafarga, M., Ribas, I., Reiners, A., et al. 2021, A&A, 652, A28
Lang, K. R., Bookbinder, J., Golub, L., & Davis, M. M. 1983, ApJ, 272, L15
Lanza, A. F. 2009, A&A, 505, 339
Lanza, A. F. 2012, A&A, 544, A23
Leggett, S. K. 1992, ApJS, 82, 351
Lépine, S., Hilton, E. J., Mann, A. W., et al. 2013, AJ, 145, 102
Liller, W. 1952, PASP, 67, 129
Lindegren, L., Hernández, J., Bombrun, A., et al. 2018, A&A, 616, A2
Lippincott, S. L. 1969, AJ, 74, 224
Lisogorskyi, M., Jones, H. R. A., & Feng, F. 2019, MNRAS, 485, 4804
Lo Curto, G., Pepe, F., Avila, G., et al. 2015, The Messenger, 162, 9
López-Santiago, J., Montes, D., Gálvez-Ortiz, M. C., et al. 2010, A&A, 514, A97
Luger, R., Foreman-Mackey, D., & Hedges, C. 2021, AJ, 162, 124
MacConnell, D. J. 1968, ApJ, 153, 313
Mahadevan, S., Ramsey, L., Bender, C., et al. 2012, SPIE Conf. Ser., 8446, 84461S
Mahadevan, S., Ramsey, L. W., Terrien, R., et al. 2014, SPIE Conf. Ser., 9147, 91471G
Mahmud, N. I., Crockett, C. J., Johns-Krull, C. M., et al. 2011, ApJ, 736, 123
Mamajek, E. E., Bartlett, J. L., Seifahrt, A., et al. 2013, AJ, 146, 154
Mann, A. W., Feiden, G. A., Gaidos, E., Boyajian, T., & von Braun, K. 2015, ApJ, 804, 64
Marfil, E., Tabernero, H. M., Montes, D., et al. 2021, A&A, 656, A162
Martin, J., Fuhrmeister, B., Mittag, M., et al. 2017, A&A, 605, A113
Mason, B. D., Wycoff, G. L., Hartkopf, W. I., Douglass, G. G., & Worley, C. E. 2001, AJ, 122, 3466
Mayor, M., Pepe, F., Queloz, D., et al. 2003, The Messenger, 114, 20
McQuillan, A., Mazeh, T., & Aigrain, S. 2013, ApJ, 775, L11
Melrose, D. B., & Dulk, G. A. 1982, ApJ, 259, 844
Merrill, P. W., Deutsch, A. J., & Keenan, P. C. 1962, ApJ, 136, 21
Meshkat, T., Mawet, D., Bryan, M. L., et al. 2017, AJ, 154, 245
Montes, D., López-Santiago, J., Gálvez, M. C., et al. 2001, MNRAS, 328, 45
Morin, J., Donati, J. F., Petit, P., et al. 2008, MNRAS, 390, 567
Mortier, A., & Collier Cameron, A. 2017, A&A, 601, A110
Mortier, A., Faria, J. P., Correia, C. M., Santerne, A., & Santos, N. C. 2015, A&A, 573, A101
Muheki, P., Guenther, E. W., Mutabazi, T., & Jurua, E. 2020, A&A, 637, A13
Namekata, K., Maehara, H., Sasaki, R., et al. 2020, PASJ, 72, 68
Newton, E. R., Irwin, J., Charbonneau, D., Berta-Thompson, Z. K., & Dittmann, J. A. 2016, ApJ, 821, L19
Ning, B., Wise, A., Cisewski-Kehe, J., Dodson-Robinson, S., & Fischer, D. 2019, AJ, 158, 210
Oliva, E., Origlia, L., Baffa, C., et al. 2006, SPIE Conf. Ser., 6269, 626919
Osten, R. A., & Bastian, T. S. 2008, ApJ, 674, 1078
Parviainen, H., Palle, E., Zapatero-Osorio, M. R., et al. 2021, A&A, 645, A16
Passegger, V. M., Schweitzer, A., Shulyak, D., et al. 2019, A&A, 627, A161
Pepe, F., Cristiani, S., Rebolo, R., et al. 2021, A&A, 645, A96
Perdelwitz, V., Mittag, M., Tal-Or, L., et al. 2021, A&A, 652, A116
Pérez-Torres, M., Gómez, J. F., Ortiz, J. L., et al. 2021, A&A, 645, A77
Perger, M., Anglada-Escudé, G., Ribas, I., et al. 2021, A&A, 645, A58
Pettersen, B. R., Coleman, L. A., & Evans, D. S. 1984, ApJS, 54, 375
Porter, J., Yowell, E., & Smith, E. 1915, Publ. Cincinnati Observ., 18, 1
Quirrenbach, A., Amado, P. J., Caballero, J. A., et al. 2014, Proc. SPIE 9147, 91471F
Quirrenbach, A., Amado, P. J., Ribas, I., et al. 2018, SPIE Conf. Ser., 10702, 107020W
Quirrenbach, A., Passegger, V. M., Trifonov, T., et al. 2022, A&A, 663, A48
Rajpaul, V., Aigrain, S., Osborne, M. A., Reece, S., & Roberts, S. 2015, MNRAS, 452, 2269
Rauer, H., Gebauer, S., Paris, P. V., et al. 2011, A&A, 529, A8
Reiners, A., Bean, J. L., Huber, K. F., et al. 2010, ApJ, 710, 432
Reiners, A., Shulyak, D., Anglada-Escudé, G., et al. 2013, A&A, 552, A103
Reiners, A., Zechmeister, M., Caballero, J. A., et al. 2018, A&A, 612, A49
Reiners, A., Shulyak, D., Käpylä, P. J., et al. 2022, A&A, 662, A41
Reuyl, D. 1943, ApJ, 97, 186
Robertson, P., Roy, A., & Mahadevan, S. 2015, ApJ, 805, L22
Robertson, P., Bender, C., Mahadevan, S., Roy, A., & Ramsey, L. W. 2016, ApJ, 832, 112
Robertson, P., Stefansson, G., Mahadevan, S., et al. 2020, ApJ, 897, 125
Robinson, R. D., Slee, O. B., & Little, A. G. 1976, ApJ, 203, L91
Rojas-Ayala, B., Covey, K. R., Muirhead, P. S., & Lloyd, J. P. 2012, ApJ, 748, 93
Rosich, A., Herrero, E., Mallonn, M., et al. 2020, A&A, 641, A82
Saar, S. H., & Linsky, J. L. 1985, ApJ, 299, L47
Sanz-Forcada, J., & Micela, G. 2002, A&A, 394, 653
Sarkis, P., Henning, T., Kürster, M., et al. 2018, AJ, 155, 257
Schöfer, P., Jeffers, S. V., Reiners, A., et al. 2019, A&A, 623, A44
Schweitzer, A., Passegger, V. M., Cifuentes, C., et al. 2019, A&A, 625, A68
Seifahrt, A., Stürmer, J., Bean, J. L., & Schwab, C. 2018, SPIE Conf. Ser., 10702, 107026D
Seifahrt, A., Bean, J. L., Stürmer, J., et al. 2020, SPIE Conf. Ser., 11447, 114471F
Shkolnik, E., Liu, M. C., & Reid, I. N. 2009, ApJ, 699, 649
Skrutskie, M. F., Cutri, R. M., Stiening, R., et al. 2006, AJ, 131, 1163
Speagle, J. S. 2020, MNRAS, 493, 3132
Speagle, J., & Barbary, K. 2018, dynesty: Dynamic Nested Sampling package, Astrophysics Source Code Library, [record ascl:1809.013]
Stepanov, A. V., Kliem, B., Zaitsev, V. V., et al. 2001, A&A, 374, 1072
Stephenson, C. B. 1986, AJ, 92, 139
Stock, S., & Kemmer, J. 2020, J. Open Source Softw., 5, 1771
Stock, S., Kemmer, J., Reffert, S., et al. 2020, A&A, 636, A119
Stock, S., Kemmer, J., Kossakowski, D., et al. 2022, A&A, submitted
Suárez Mascareño, A., Faria, J. P., Figueira, P., et al. 2020, A&A, 639, A77
Tal-Or, L., Zechmeister, M., Reiners, A., et al. 2018, A&A, 614, A122
Tal-Or, L., Trifonov, T., Zucker, S., Mazeh, T., & Zechmeister, M. 2019, MNRAS, 484, L8
Tamura, M., Suto, H., Nishikawa, J., et al. 2012, SPIE Conf. Ser., 8446, 84461T
Teitler, S., & Königl, A. 2014, ApJ, 786, 139
Thompson, A. P. G., Watson, C. A., Haywood, R. D., et al. 2020, MNRAS, 494, 4279
Tofflemire, B. M., Wisniewski, J. P., Kowalski, A. F., et al. 2012, AJ, 143, 12
Trifonov, T., Tal-Or, L., Zechmeister, M., et al. 2020, A&A, 636, A74
Trotta, R. 2008, Contemp. Phys., 49, 71
Tuomi, M., Jones, H. R. A., Barnes, J. R., et al. 2018, AJ, 155, 192
Turnpenney, S., Nichols, J. D., Wynn, G. A., & Casewell, S. L. 2017, MNRAS, 470, 4274
van de Kamp, P., & Lippincott, S. L. 1949, AJ, 55, 16
van Leeuwen, F. 2007, A&A, 474, 653
Vidotto, A. A., Jardine, M., Morin, J., et al. 2013, A&A, 557, A67
Villadsen, J., & Hallinan, G. 2019, ApJ, 871, 214
Vogt, S. S., Allen, S. L., Bigelow, B. C., et al. 1994, Proc. SPIE, 2198, 362
Walkowicz, L. M., & Basri, G. S. 2013, MNRAS, 436, 1883
Wise, A. W., Dodson-Robinson, S. E., Bevenour, K., & Provini, A. 2018, AJ, 156, 180
Zechmeister, M., & Kürster, M. 2009, A&A, 496, 577
Zechmeister, M., Reiners, A., Amado, P. J., et al. 2018, A&A, 609, A12
Zucker, S., & Mazeh, T. 1994, ApJ, 420, 806

Appendix A: RV data and short tables

Table A.1. Published rotational periods values of AD Leo[a].

Data	P_{rot} (d)	Reference
Photometry		
TESS-s48	2.2304 ± 0.0014	This work[b]
STELLA	2.237 ± 0.035	C20
ASAS-N	$2.22791^{+0.00066}_{-0.00055}$	T18[c]
MOST-1	2.289 ± 0.019	T18[d]
MOST-2	2.145 ± 0.011	T18[d]
MOST	$2.23^{+0.36}_{-0.27}$	Hun2012
FCAPT	2.23	Eng2009
Spectroscopy		
HP2	2.2249	R20[e]
HT1	2.2244 ± 0.0010	C20
HT2	2.2225 ± 0.0044	C20
G1 + G2	2.2246 ± 0.0219	C20[f]
HARPS + HIRES	$2.22567^{+0.00026}_{-0.00011}$	T18
HARPS	2.22704	Rei2013[g]
HARPS	2.2267 ± 0.0001	Bon2013
Tomography		
ESPaDOnS + NARVAL	2.2399 ± 0.0006	Mor2008

Notes. [(a)]The P_{rot} determined by us from the GP component of the best-fit model on the spectroscopic data (Sect 6.3, Table 3) is $2.2270^{+0.0010}_{-0.0011}$ d. [(b)]See Sect. 2.2 for the analysis setup. [(c)]After subtraction of a longer periodicity in the data, see reference for details. [(d)]The *MOST* baseline of 8.9 days was separated into two independent data sets, see reference for details. [(e)]Value was not explicitly included in the text but appeared in the RV phase-folded plot. [(f)]A narrowly constrained Gaussian prior of 2.225 ± 0.020 d was used to detect a 3σ upper limit of $K = 23\,\mathrm{m\,s^{-1}}$. [(g)]Value based off of the most prominent peak in the periodogram.

References. Bon2013: Bonfils et al. (2013); Eng2009: Engle et al. (2009); Hun2012: Hunt-Walker et al. (2012); Mor2008: Morin et al. (2008); Rei2013: Reiners et al. (2013).

Table A.2. CARMENES VIS RV data of AD Leo.

BJD (TDB*)	RV ($\mathrm{m\,s^{-1}}$)	σ_{RV} ($\mathrm{m\,s^{-1}}$)
2458199.31070	17.26	3.18
2458199.43446	−0.85	2.68
2458199.53410	−7.02	2.70
2458200.30763	−13.30	1.61
2458200.33569	−12.72	1.91
2458200.52737	−0.81	2.85
2458205.33771	18.22	1.62
2458205.43139	23.51	1.59
2458205.57006	24.40	2.42
2458209.35609	−6.66	1.37
2458209.47549	3.29	1.75
2458210.31450	21.81	7.25
2458211.33225	−15.82	4.55
2458211.33586	−12.85	3.16
2458212.36090	32.09	2.45
2458212.56685	25.08	2.78
2458213.41097	−23.28	2.34
2458213.51416	−22.32	2.31
2458215.31521	−22.16	2.03
2458215.44196	−31.14	2.08
2458215.54733	−25.31	2.17
2458216.36673	5.91	3.27
2458217.35751	−7.13	3.32
2458218.35496	−8.17	4.46
2458225.34239	9.43	1.61
2458225.57485	24.92	2.99
2458893.39518	21.10	2.58
2458893.39739	18.67	2.96
2458893.56436	18.29	2.49
2458893.56616	16.85	2.35
2458893.69412	14.18	2.18
2458893.69600	14.00	1.91
2458894.39429	−14.04	2.12
2458894.39632	−9.74	2.55
2458894.40312	−12.89	2.22
2458894.40435	−12.00	2.12
2458894.55514	−15.42	1.90
2458894.55639	−17.37	1.86
2458894.70318	−16.27	2.50
2458894.70436	−15.28	2.15
2458895.38983	11.95	2.90
2458895.39120	7.18	2.46
2458895.54067	14.16	2.47
2458895.54207	16.96	2.62
2458895.71912	21.55	3.84
2458895.72044	16.96	3.15

Notes. [(*)]Barycentric dynamical time.

Table A.3. CARMENES NIR RV data of AD Leo.

BJD (TDB*)	RV ($m\,s^{-1}$)	σ_{RV} ($m\,s^{-1}$)
2458199.31074	−9.74	9.77
2458199.43432	−1.48	9.80
2458199.53395	−21.53	7.61
2458200.30763	−16.58	5.70
2458200.33556	−24.46	6.47
2458200.52732	5.43	24.79
2458205.33748	13.42	6.57
2458205.43117	27.81	5.84
2458205.57007	9.75	5.85
2458209.35584	−5.05	5.92
2458209.47579	−11.00	7.33
2458210.31440	−5.64	23.89
2458211.33294	−24.69	13.57
2458211.33596	−21.72	9.17
2458212.36111	26.48	5.11
2458212.56689	7.25	7.70
2458213.41095	−14.93	6.10
2458213.51413	−16.77	5.91
2458215.31521	−7.97	4.84
2458215.44212	−6.86	5.62
2458215.54747	−11.64	7.33
2458216.36658	−7.24	9.65
2458217.35744	6.59	23.42
2458218.35494	−9.44	11.83
2458225.34234	10.32	7.20
2458225.57469	−1.85	10.24
2458893.39513	17.18	5.81
2458893.39739	31.12	12.16
2458893.56431	8.59	7.67
2458893.56616	6.39	10.36
2458893.69395	−2.56	11.05
2458893.69590	15.99	13.10
2458894.39425	−1.52	7.95
2458894.39614	−3.07	12.02
2458894.40311	15.02	8.90
2458894.40428	0.83	6.93
2458894.55510	−2.68	7.32
2458894.55633	−13.38	7.02
2458894.70320	−27.15	11.60
2458894.70442	−15.44	39.11
2458895.38980	18.25	6.22
2458895.39117	2.50	8.46
2458895.54064	10.29	7.53
2458895.54203	−1.03	10.48
2458895.71911	13.87	14.45
2458895.72021	5.28	18.57

Notes. (*)Barycentric dynamical time.

Table A.4. HARPS RV and accompanying data for AD Leo used in this paper, first processed using `serval` (Zechmeister et al. 2018) and then corrected for nightly zero points (Trifonov et al. 2020).

BJD (TDB*)	RV ($m\,s^{-1}$)	σ_{RV} ($m\,s^{-1}$)
2452986.859	28.07	1.89
2453511.548	−19.61	1.01
2453520.521	−15.62	1.00
2453543.482	13.69	1.26
2453544.453	−9.50	0.92
2453550.460	39.00	2.32
2453728.866	39.05	1.03
2453758.755	−21.83	0.74
2453760.755	−12.09	0.76
2453761.781	18.34	0.67
2453783.726	−7.40	0.70
2453785.727	−18.55	0.69
2453809.661	−2.50	0.56
2453810.677	10.93	0.68
2453811.676	8.04	0.66
2453812.664	−9.53	0.96
2453813.659	20.68	0.66
2453814.655	−20.46	0.85
2453815.571	26.14	0.72
2453815.622	25.40	0.66
2453815.736	24.43	0.63
2453816.544	−14.43	0.74
2453816.656	−19.40	0.65
2453816.722	−21.99	0.68
2453817.551	24.31	0.63
2453817.676	26.22	0.67
2453829.615	−1.07	0.62
2453830.540	−7.15	0.79
2453831.670	8.61	0.57
2453832.650	−11.77	0.62
2453833.628	23.40	0.57
2453834.611	−27.06	0.63
2453835.656	27.56	0.63
2453836.617	−19.54	0.59
2453861.594	−1.22	0.69
2453863.569	−22.08	0.69
2453864.535	29.03	0.66
2453867.542	−13.93	0.69
2453868.518	22.20	0.70
2453871.563	19.01	0.62
2456656.850	−36.79	0.87
2456656.861	−35.19	0.86
2456657.853	39.91	0.88
2456658.865	−45.31	0.88
2456658.876	−45.60	0.86
2456659.859	43.23	1.17
2456797.513	−29.24	0.57

Notes. (*)Barycentric dynamical time.

Table A.5. HIRES RV data for AD Leo used in this paper produced by Tal-Or et al. (2019).

BJD (TDB*)	RV ($m\,s^{-1}$)	σ_{RV} ($m\,s^{-1}$)
2452064.85709	−4.47	2.24
2452334.01660	28.75	1.89
2452602.13013	−17.43	1.94
2452652.10228	8.91	1.97
2452653.01007	−5.16	1.98
2452711.93243	−4.57	1.80
2452712.95569	−5.29	2.08
2452804.84095	−14.89	2.40
2452828.76276	5.11	2.12
2453044.88295	17.33	2.10
2453339.12059	13.73	2.02
2453340.13691	−24.87	2.03
2453398.91738	16.05	1.94
2453398.92487	12.70	1.82
2453724.00531	22.43	2.11
2453724.01159	20.59	1.88
2453748.00269	−21.62	1.73
2453749.89640	−21.39	1.72
2453749.90307	−24.10	1.83
2453750.91326	15.30	1.55
2453751.93398	−12.65	3.19
2453753.00706	17.96	1.75
2453753.01294	28.22	2.16
2453753.94933	−12.15	1.71
2453753.95561	−9.32	1.73
2453776.07390	−0.55	1.69
2453776.08012	−0.77	1.59
2453777.06086	−22.01	1.65
2453777.06716	−17.44	1.73
2453777.88577	8.69	1.56
2453778.14548	0.71	1.79
2453778.82453	−26.82	1.71
2453837.86778	19.00	1.99
2453837.87490	17.74	1.83
2453841.86395	10.58	1.91
2453841.87031	8.42	1.79
2454130.10052	−36.01	1.90
2454130.10671	−37.32	1.90
2454130.99591	5.96	2.17
2454490.99221	−31.71	1.93
2455197.95670	26.65	2.73
2455905.11046	−31.07	2.00
2456641.07001	−58.13	1.94

Notes. (*)Barycentric dynamical time.

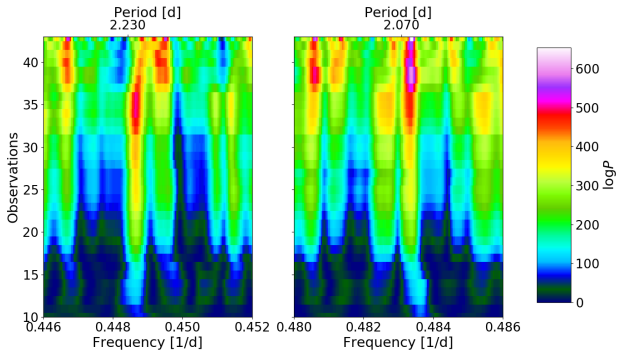

Fig. B.1. S-BGLS periodograms of the HIRES data of AD Leo, zoomed into two frequency ranges (left, 2.23 days, and right, 2.07 d) for the HIRES data. The nominal value log P does not carry significance, rather the relative values of log P are of importance.

Appendix B: Aliasing in HIRES data

The periodogram of the HIRES data set as a whole exhibits the strongest peak at 2.07 d. instead of at 2.23 days (see Fig. B.1). This can be understood as the window function has a peak at 1 month, more specifically, 29.53 days; 2.07 days and 2.23 days are thus an alias pair with respect to this period. As in Dawson & Fabrycky (2010) and Stock et al. (2020), a dealiasing approach using the `AliasFinder`[22] (Stock & Kemmer 2020) was performed. However, probably due to the fact that the underlying signal may not be a simple sinusoid, but rather a quasi-periodic signal with varying amplitudes and phaseshifts, the results were not fully conclusive. To further investigate, we performed a stacked Bayesian GLS (s-BGLS) periodogram (see Fig. B.1) where the stacking enables us to determine the coherence of a signal with increasing number of observations (Mortier et al. 2015; Mortier & Collier Cameron 2017). As Mortier & Collier Cameron (2017), we normalized all s-BGLS periodograms to their respective minimum values, with the minimum probability set to 1. We found that until about 35 data points, which corresponds to the start of the sparse data, the 2.23 days signal seems to be the most prominent. Afterwards, the alias at 2.07 d gains significance. This behavior is in accordance to what we expect from an unstable, incoherent signal: when one signal loses significance, another one gains it (as also demonstrated Mortier & Collier Cameron 2017, with the Sun as an example). We conclude that the HIRES data are fully consistent with an RV modulation with a 2.23 days period.

[22] https://github.com/JonasKemmer/AliasFinder

Appendix C: Stellar activity

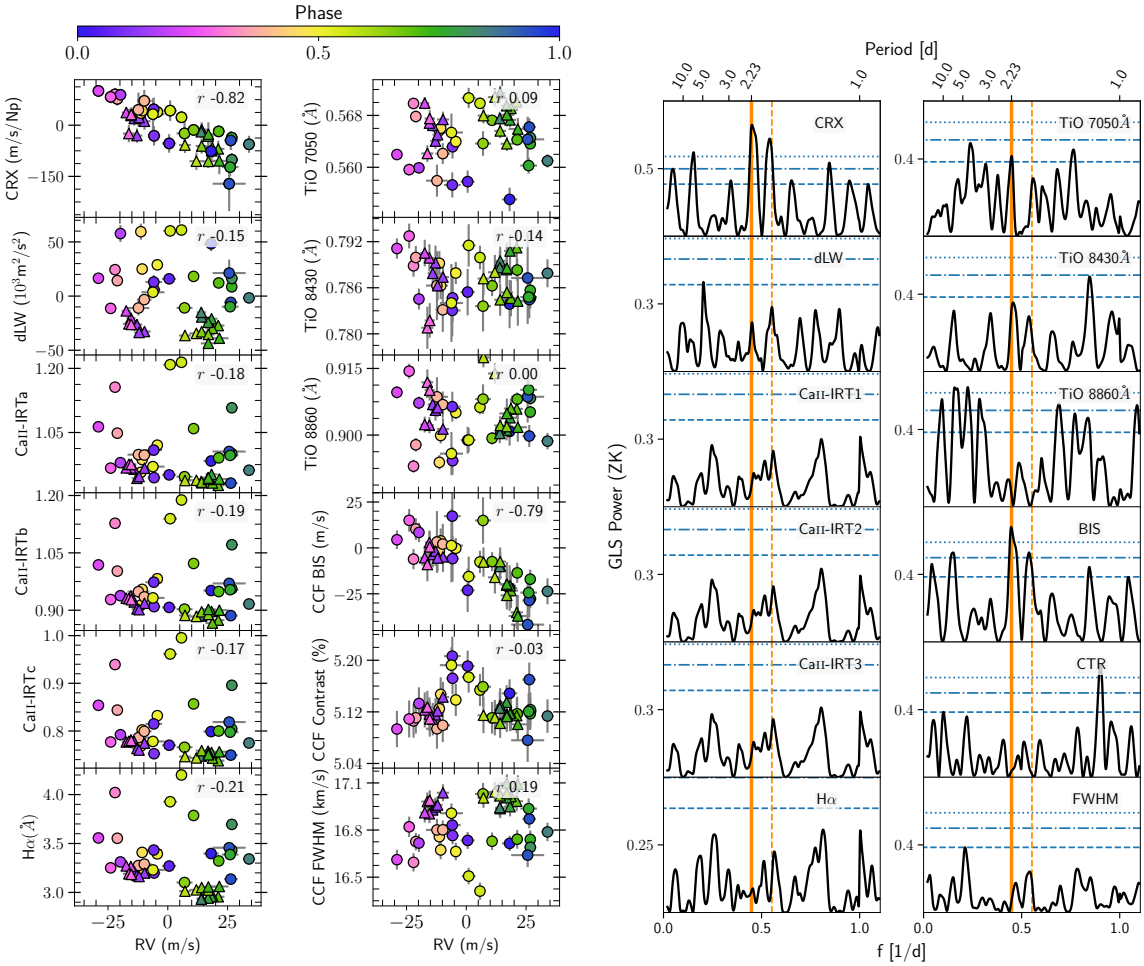

Fig. C.1. Correlation plots with the RVs (*left*) and GLS periodograms (*right*) of the various stellar activity indicators from the CARMENES VIS spectroscopic data for AD Leo. For the correlation plots, the circles and triangles represent the first and second subset of CARMENES VIS data, respectively. Data points are color-coded with the rotation phase. The Pearson-r correlation coefficient combining both subsets is shown within each panel (R). For the periodograms, only the first season of the CARMENES VIS data was considered for plotting. The orange vertical solid and dashed lines represent the rotation period at $P = 2.23$ d and its daily alias at 1.81 d. The horizontal dotted, dot-dashed, and dashed blue lines represent the 10%, 1%, and 0.1% FAP levels.

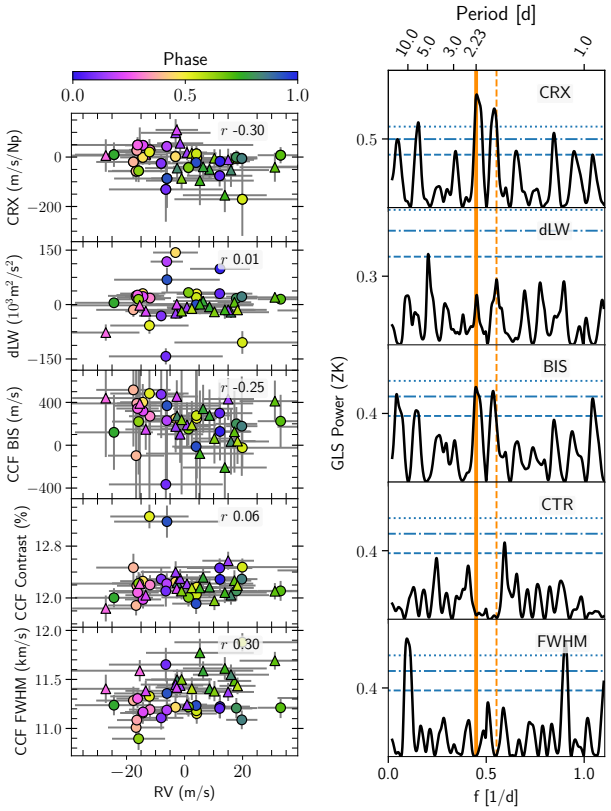

Fig. C.2. Same as in Fig. C.1, but for the CARMENES NIR channel.

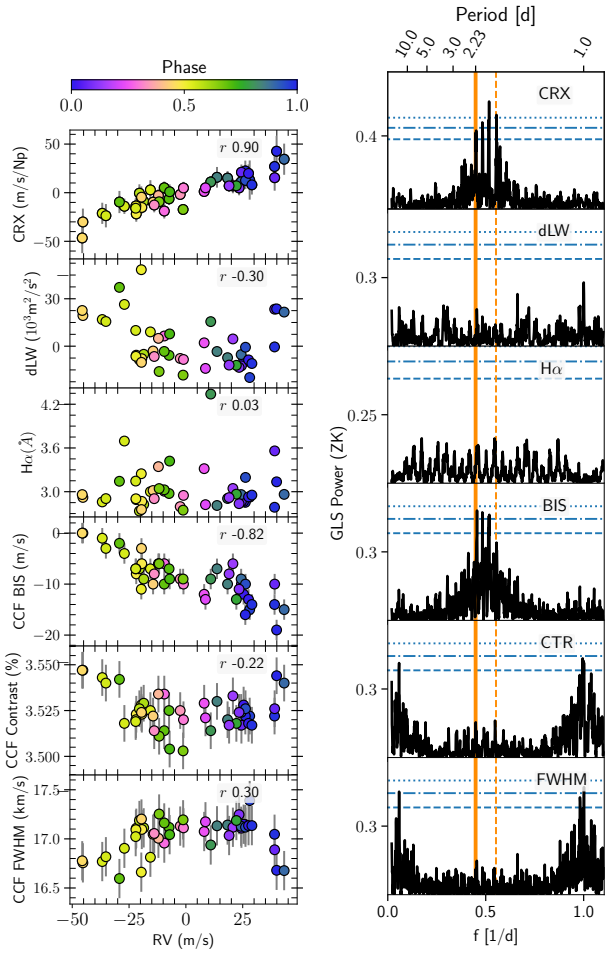

Fig. C.3. Same as in Fig. C.1, but for the HARPS instrument.